



Science Arts & Métiers (SAM)

is an open access repository that collects the work of Arts et Métiers Institute of Technology researchers and makes it freely available over the web where possible.

This is an author-deposited version published in: <https://sam.ensam.eu>
Handle ID: <http://hdl.handle.net/10985/17517>

To cite this version :

C TENAUD, B PODVIN, Y FRAIGNEAU, Virginie DARU - On wall pressure fluctuations and their coupling with vortex dynamics in a separated reattached turbulent flow over a blunt flat plate - International Journal of Heat and Fluid Flow - Vol. 61, p.730-748 - 2016

Any correspondence concerning this service should be sent to the repository

Administrator : scienceouverte@ensam.eu



On wall pressure fluctuations and their coupling with vortex dynamics in a separated–reattached turbulent flow over a blunt flat plate

C. Tenaud^{a,*}, B. Podvin^a, Y. Fraigneau^a, V. Daru^{b,a}

^aLIMSI, CNRS, Université Paris-Saclay, Bât 508, Rue John Von Neumann, F-91403 ORSAY Cedex, France

^bLaboratoire DynFluid, Arts & Métiers ParisTech, 151 Boulevard de l'Hôpital, F-75013 Paris, FRANCE

A B S T R A C T

This study deals with the numerical predictions through Large-Eddy Simulation (LES) of the separated–reattached turbulent flow over a blunt flat plate for analyzing main coherent structure features and their relation to the unsteady pressure field. A compressible approach that inherently includes acoustic propagation is here followed to describe the relationship between pressure fluctuations and vortex dynamics around the separation bubble. The objective of the present work is then to contribute to a better understanding of the coupling between the vortex dynamics and the wall pressure fluctuations. The filtered compressible Navier–Stokes equations are then solved with a numerical method that follows a Lax–Wendroff approach to recover a high accuracy in both time and space. For validations, the present numerical results are compared to experimental measurements, coming from both the Pprime laboratory (Sicot et al., 2012) and the literature (Cherry et al., 1984; Kiya and Sasaki, 1985; Tafti and Vanka, 1991; Sicot et al., 2012). Our numerical results very well predict mean and fluctuating pressure and velocity fields. Flapping, shedding as well as Kelvin–Helmholtz characteristic frequencies deduced by present simulations are in very good agreement with the experimental values generally admitted. These characteristic modes are also visible on unsteady pressure signatures even far away from the separation. Spectral, POD and EPOD (extended POD) analyses are then applied to these numerical data to enhance the salient features of the pressure and velocity fields, especially the unsteady wall pressure in connection with either the vortex shedding or the low frequency shear-layer flapping. A contribution to the understanding of the coupling between wall pressure fluctuations and eddy vortices is finally proposed.

Keywords:

High-order scheme
Unsteady flow
Turbulence
LES
Pressure fluctuations
Vortex dynamics

1. Introduction

Massively separated flows have engineering concerns since they occur in many aerodynamic applications, such as around ground vehicles, train or aircraft bodies. Such flow configurations are highly 3D and mainly unsteady with however well-known characteristic frequencies. One of fundamental issues relates to the mechanisms driving the acoustic propagation in the far field surrounding these aerodynamic bodies. Another one is the sound propagation toward the interior of the vehicle since main sound frequencies occur on the same range as the voice frequencies. If one wants to control acoustic disturbances and develop noise reduction process applied to a quiet vehicle, it is first essential to better understand the mechanisms involved in the noise generation and its transmission toward the habitacle. Sources of noise are essentially due to the coupling between eddy structures and

the unsteady pressure field in the core of the flow (Hoarau et al., 2006). A major challenge is therefore to accurately predict the pressure fluctuations generated within the flow that is central to the acoustic source generation along the solid surfaces. This study is hence devoted to a better understanding of the production of fluctuating pressures on a solid wall on which a massively separated flow impinges. We here deal with the numerical simulation of the turbulent flow generated around a blunt flat plate with a sharp leading edge. This configuration constitutes an academic model for studying the main features of massively separated–reattached turbulent flows, encountered for instance around vehicles, mainly in the vicinity of the front hood or close to the window or door post of a car.

In the past, this configuration has widely been studied experimentally. Numerous experimental results are available in the literature on the structure of turbulent flow separation bubbles and its relaxation after the reattachment (Castro and Epik, 1998; Castro and Haque, 1987; Cherry et al., 1984; Eaton and Johnston, 1981; Hoarau et al., 2006; Kiya and Sasaki, 1983; 1985; Sicot et al., 2012). The dynamics of the separation bubble and its reattachment have

* Corresponding author. Fax: +33 1 69 85 80 88.

E-mail address: Christian.Tenaud@limsi.fr (C. Tenaud).

mainly been reviewed on both the flow along a side of a blunt flat plate and the backward-facing step flow field. The structure of large scale vortices have been studied by Hillier and Cherry (1981); Kiya and Sasaki (1983, 1985) and Cherry et al. (1984) that educe the main mechanisms involved in the separation bubble dynamics. They showed that the flow in the separation bubble is governed by two main mechanisms: the *shedding* of large-scale vortices downstream of the separation and a low-frequency unsteadiness called *flapping*, linked to the shredding and enlargement of the bubble. The role of the shear layer edging the separation in the bubble dynamics and the reattachment was also demonstrated (Castro and Epik, 1998; Castro and Haque, 1987). The connection between these main mechanisms is still not clear and deserves more results for further analysis. The three-dimensional feature of large-scale structures in the reattaching zone was underlined and its influence on the wall pressure fluctuations was studied through either cross-correlations (Kiya and Sasaki, 1983; Saathoff and Melbourne, 1997) or extended POD analysis (Hoarau et al., 2006; Sicot et al., 2012; Tran, 2012). Wall pressure fluctuations are related to the motion of large-scale vortices, especially hairpin vortices in the reattachment region that produce large amplitude fluctuations. The influence of the free-stream turbulence on the flow dynamics have also been reviewed (Castro and Epik, 1998; Saathoff and Melbourne, 1997) and an increase of turbulence intensity tends to reduce the reattachment length. Although the mean pressure was decreased at separation, the magnitude of the pressure fluctuations in the separation bubble is increased (Saathoff and Melbourne, 1997). It was however shown that “the spanwise length of vortices in the separation bubble is not directly related to longitudinal velocity fluctuations in the free-stream” (Saathoff and Melbourne, 1997). Experimental analysis also investigated the relaxation occurring downstream the reattachment. Although some characteristics (log-law for instance) of canonical boundary layers are re-established rather rapidly, the energetic *mixing-layer like* structures occurring around reattachment evolve very slowly since 70 boundary layer thicknesses are needed to recover common structures of a standard boundary layer (Castro and Epik, 1996; 1998; Sicot et al., 2012). Following these results, authors (Castro and Epik, 1996; 1998) conjectured that second order Reynolds stress models are not able to predict the slow decay of the energetic large scale structures in the outer part of the flow and its influence on the inner region. We can then think that *DNS* and resolved *LES* remain ideal tools to mimic such flow phenomena.

Unlike numerous experiments, only few numerical simulations of the flow generated around a blunt flat plate exist in the literature. Most of these computations concern low to moderate Reynolds number configurations aiming at studying steady laminar flow to unsteady regime with quasi-periodic vortices shed in the vicinity of the reattachment (Lamballais et al., 2010; Tafti and Vanka, 1991). Authors studied the curvature effects of a rounded leading edge on the dynamics of the separation (Lamballais et al., 2010). Large-Eddy Simulations have also been conducted to investigate the transitional separated-reattached flow over a flat plate (Yang and Abdalla, 2009; Yang and Voke, 2000; 2001). As far as we can note in these previous results for low and moderate Reynolds number regimes, the reattachment length seems very sensitive to the Reynolds number. Even at high Reynolds number regime, the reattachment length (L_R) does not recover a unique value since it is distributed in between [4, 5.5] (See Cherry et al., 1984 for more details). To try to explain this wide-ranging of L_R values, the influence of free-stream turbulence and surface curvature change have been reviewed on the transition process from laminar separation to reattachment in a turbulent boundary layer. At present, reasons of this broadness (Bruno et al., 2014) are still unexplained and no specific value of this length emerges from previous result, meaning that new numerical results must be provided to get a better

insight into this configuration. Nevertheless, several authors discussed the existence of vortex shedding and low frequency shear-layer flapping (Yang and Voke, 2001). Although the connection between these two main mechanisms is not completely elucidated, they postulated that two different topological structures could be associated with the normal shedding and the shedding responsible for low-frequency flapping. Another connection that needs to be elucidated is the relationship between the vortex structure dynamics and the pressure fluctuations. Ji and Wang (2010) studied the aeroacoustics of turbulent boundary layer flows over backward and forward facing small steps. By using incompressible *LES* coupled with the solution of a Green’s function following Lightill’s analogy, they analyzed frequency spectra of wall pressure to contribute to a better understanding of noise production. However, all these studies essentially concern incompressible flow simulations and to obtain a better description of the relationship between pressure fluctuations and vortex dynamics for separated-reattached flow over a flat plate, a compressible approach might be more suitable since acoustic propagation inherently included. This study is thus devoted to the numerical predictions through compressible Large-Eddy Simulation (*LES*) of the separated–reattached turbulent flow over a blunt flat plate with a right-angled leading edge. To our knowledge, there does not exist any study of compressible flow over the turbulent flow over a forward facing step which provides an analysis of the main coherent structure features and their relation to the unsteady pressure field. Hence, the objective of this work is two fold: (i) to provide a well resolved *LES* reference database for analyzing the dynamics of the main coherent structures in the separated–reattached turbulent flow over a blunt flat plate, and (ii) to contribute to a better understanding of the coupling between the vortex dynamics and the wall pressure fluctuations, especially in connection with either the vortex shedding or the low frequency shear-layer flapping.

In this work, we solve the filtered compressible Navier–Stokes equations following a *LES* approach with a dynamic vorticity model to account for subgrid scales. The governing *LES* equations and the subgrid-scale modeling are presented in Section 1. Following a Lax–Wendroff approach, the numerical method employs a 7th-order scheme introduced in Daru and Tenaud (2004, 2009), named OS7, which recovers a high accuracy in both time and space with a great efficiency in terms of CPU time compared to more conventional schemes. Numerical approximations are described in Section 2 and the numerical ingredients, including the definition of the computational domain, boundary conditions, and grid generation, are presented in Section 3. In Section 4, we then validate our numerical results by comparisons with experimental measurements, coming from both the Pprime laboratory and different experiments (Cherry et al., 1984; Kiya and Sasaki, 1985; Sicot et al., 2012; Tafti and Vanka, 1991). Thus, spectral, POD and EPOD (extended POD) analyses are applied on the present numerical data to determine the salient features of the pressure and velocity fields. A contribution to the understanding of the coupling between wall pressure fluctuations and eddy vortices is eventually proposed. Finally in Section 6, we conclude and present prospects for future work.

2. The governing *LES* equations and the subgrid-scale modeling

The governing equations are the compressible Navier–Stokes equations filtered with an implicit spatial filter (noted $\overline{(\cdot)}$) combined with the density-weighted Favre decomposition (Favre, 1965) ($\overline{(\cdot)}$). The characteristic filter size depends both on the local mesh size and on the intrinsic dissipation of the numerical scheme. This suggests to use schemes for *LES* that exhibit as low dissipation error as possible because the greater the intrinsic dissipation, the larger the size of the implicit filter.

These filtered equations can be written in different ways (Doris, 2000; Doris et al., 2000; Lenormand et al., 2000; Lesieur and Comte, 2001; Vreman et al., 1995), depending on the choice made for the resolved quantities. Though the review of Lesieur and Comte (2001) upon the use of a macro temperature and a macro pressure to simulate a channel flow, concludes that the subgrid contribution to pressure and temperature is negligible under a reasonable subgrid-scale Mach number condition, we prefer to use real pressure, temperature and energy, as Vreman et al. (1995) suggested, because LES results must be compared to experiments. According to these authors (Vreman et al., 1995), the governing equations, written in a conservative form and in cartesian coordinates, read as follows:

$$\frac{\partial \bar{\mathbf{U}}}{\partial t} + \nabla \cdot (\mathbf{F}^E(\bar{\mathbf{U}}) + \mathbf{F}^V(\bar{\mathbf{U}}, \nabla \bar{\mathbf{U}})) = 0, \quad (1)$$

where $\bar{\mathbf{U}}$ is the vector of the filtered conservative variables and \mathbf{F}^E and \mathbf{F}^V are the Euler and the viscous vector fluxes, respectively:

$$\bar{\mathbf{U}} = \begin{pmatrix} \bar{\rho} \\ \bar{\rho} \tilde{\mathbf{v}} \\ \bar{\rho} \tilde{E} \end{pmatrix}; \mathbf{F}^E = \begin{pmatrix} \bar{\rho} \tilde{\mathbf{v}} \\ \bar{\rho} \tilde{\mathbf{v}} \otimes \tilde{\mathbf{v}} + \frac{\bar{P}}{\gamma M_0^2} \mathbb{I} \\ \bar{\rho} \tilde{\mathbf{v}} \tilde{E} + \tilde{\mathbf{v}} \frac{\bar{P}}{\gamma M_0^2} \end{pmatrix}; \quad (2)$$

$$\mathbf{F}^V = \begin{pmatrix} 0 \\ \sigma + \tau \\ \tilde{\mathbf{v}}(\sigma + \tau) - \tilde{\mathbf{q}} - \psi \end{pmatrix}.$$

These equations are written in a dimensionless form by using the reference values of the density (ρ_0), the velocity (v_0), and the length scale (L_0). In terms of large scales, $\bar{\rho}$ is the filtered density of the fluid, $\tilde{\mathbf{v}} = \{\tilde{v}_i\}^t$ ($i \in [13]$) is the density-weighted filtered velocity vector, \bar{P} is the filtered static pressure and \tilde{E} is the density-weighted filtered total energy per unit of mass. The resolved stress tensor (σ) and the resolved heat flux ($\tilde{\mathbf{q}}$) are respectively given by:

$$\sigma = -\frac{\tilde{\mu}}{Re} \left(\nabla \tilde{\mathbf{v}} + \nabla^t \tilde{\mathbf{v}} - \frac{2}{3} \nabla \cdot \tilde{\mathbf{v}} \mathbb{I} \right), \quad (3)$$

$$\tilde{\mathbf{q}} = -\frac{\tilde{\mu}}{(\gamma - 1) Re Pr M_0^2} \nabla \tilde{T}, \quad (4)$$

where $\tilde{\mu}$ is the dimensionless dynamic viscosity related to the resolved static temperature \tilde{T} by a Sutherland's law:

$$\tilde{\mu}(\tilde{T}) = \tilde{T}^{\frac{3}{2}} \frac{1 + \frac{110.4}{T_0}}{\tilde{T} + \frac{110.4}{T_0}}, \quad (5)$$

T_0 being the reference temperature. The resolved pressure and temperature are expressed in terms of the conservative quantities by using an equation of state:

$$\bar{P} = (\gamma - 1) \left[\bar{\rho} \tilde{E} - \frac{1}{2} \bar{\rho} \tilde{\mathbf{v}} \cdot \tilde{\mathbf{v}} - \tau : \mathbb{I} \right], \quad (6)$$

$$\tilde{T} = \frac{\bar{P}}{\bar{\rho}}. \quad (7)$$

This study is restricted to an ideal gas with a constant specific heat ratio $\gamma = 1.4$ and a constant Prandtl number $Pr = 0.73$, for air. The Reynolds number is based on the reference values: $Re = \rho_0 v_0 L_0 / \mu(T_0)$. $M_0 = v_0 / (\gamma R T_0)$ is the Mach number (R is the constant of the gas, $R = 287 \text{ J.Kg}^{-1}.\text{K}^{-1}$ for air).

2.1. Subgrid-scale modeling

The two subgrid-scale contributions, i.e. the subgrid stress tensor:

$$\tau = (\bar{\rho} \mathbf{v} \otimes \mathbf{v} - \bar{\rho} \tilde{\mathbf{v}} \otimes \tilde{\mathbf{v}}), \quad (8)$$

and the subgrid heat flux:

$$\psi = \frac{1}{(\gamma - 1) M_0^2} (\bar{\rho} \mathbf{v} T - \bar{\rho} \tilde{\mathbf{v}} \tilde{T}), \quad (9)$$

need to be related to the resolved part of the quantities by means of modelings that are presented hereafter.

2.1.1. Model of the subgrid stress tensor

To account for the kinetic energy dissipation occurring at small-scales, the model of the subgrid stress tensor (τ) assumes the energy transfer theory. τ is then evaluated by a Boussinesq hypothesis, meaning that the deviatoric part of the subgrid-scale tensor is related to the strain rate tensor of the resolved velocity field by using a subgrid viscosity (μ_{sg}):

$$-\tau + \frac{1}{3} tr(\tau) \mathbb{I} = \mu_{sg} \left(\nabla \tilde{\mathbf{v}} + \nabla^t \tilde{\mathbf{v}} - \frac{2}{3} \nabla \cdot \tilde{\mathbf{v}} \mathbb{I} \right), \quad (10)$$

where $tr(\cdot)$ denotes the tensor trace. The subgrid viscosity model must mimic the dissipative exchanges between the small and the large scale structures. This viscosity should result from the product of a length scale and a time scale representative of the small scale structures.

In this study, two sub-grid scale models have been employed to enhanced the influence of sub-grid modelings on results: (i) a mixed scale model, initially developed by Sagaut (1995, 1998) for incompressible flow calculations and derived for compressible flows in Tenaud and Ta Phuoc (1997); and (ii) a more sophisticated model using a Smagorinsky model (Smagorinsky, 1963) with a dynamic procedure (Germano et al., 1991).

2.1.1.1. Mixed scale model. The mixed scale model was introduced to improve the behavior of the basic vorticity model that is questionable in turbulent regions where the dissipative length scale is greater than the estimate of the filter cut-off length scale. The mixed scale model is derived from a class of models which supposed that the subgrid viscosity is a function of the transfer rate of the kinetic energy, the kinetic energy at the cut-off and the cut-off wave number. Following a dimensional analysis and assuming a local spectral equilibrium, we may obtain a one parameter family model, written in the physical space as the algebraic average of the vorticity model (Mansour et al., 1978) and the TKE model (TKE: Turbulent Kinetic Energy) (Bardina et al., 1980):

$$\mu_{sg} = \left(\underbrace{\bar{\rho} C_\omega^2 \bar{\Delta}^2 \|\bar{\omega}\|}_{\mu_\omega} \right)^\alpha \left(\underbrace{\bar{\rho} C_B \bar{\Delta} \sqrt{q_c}}_{\mu_k} \right)^{(1-\alpha)}. \quad (11)$$

We took $\alpha = 1/2$, in agreement with simulations carried out with this model so far (see Lenormand et al., 2000; Sagaut, 1998; Tenaud and Ta Phuoc, 1997). C_ω and C_B are respectively the constant of the vorticity (Mansour et al., 1978) and the TKE (Bardina et al., 1980) models. In practice, common values of C_ω are: $C_\omega \in [0.1, 0.12]$ (Deardorff, 1970; Meneveau, 1994; O'Neil and Meneveau, 1997) and, to respect galilean invariance, $C_B = 1$. (Bardina et al., 1980). Following Bardina et al. (1980) about the TKE model, this velocity scale has been related to the subgrid kinetic energy by using a scale similarity assumption. Thanks to an analytical test filter (\cdot) with a cut-off length scale $\hat{\Delta}$ larger than $\bar{\Delta}$, the subgrid scale velocity is estimated by using the subgrid kinetic energy at the highest resolved wave numbers (q_c):

$$\|\mathbf{u}''\| := \sqrt{q_c} = \sqrt{\frac{1}{2} (\tilde{v} - \hat{v}) \cdot (\tilde{v} - \hat{v})}.$$

In the followings, the explicit test filter is typically expressed using a trapezoidal rule (Liu et al., 1994) and $\hat{\Delta} = 2.\bar{\Delta}$.

Besides the modeling of the subgrid viscosity, one must provide a model of the trace of the subgrid tensor, appearing in the Boussinesq formulae (10). To be consistent with the scale similarity assumption previously made, $tr(\tau)$ is expressed as a function of the subgrid kinetic energy (q_c):

$$tr(\tau) = 2 \bar{\rho} q_c. \quad (12)$$

LES of several test-cases at high Reynolds number were already performed successfully with the mixed scale model, as for instance the simulation of a 3D spatial mixing layer (Doris et al., 2000) or the simulation of a compressible jet (Ferreira Gago et al., 2002). Moreover, an analysis of the behavior of this model in the bounded flow test-case of the temporal channel flow has been proposed by Lenormand et al. (2000).

2.1.1.2. Dynamical subgrid-scale model. The dynamical subgrid-scale model based on the Germano's procedure (Germano, 1992; Germano et al., 1991), has been developed to better account for the local flow structure and to improve the modeling of the anisotropic behavior. The model is deduced from the relationship between subgrid stress tensors evaluated at two filtering grid levels. Considering τ as the subgrid stress tensor coming from the implicit filtering procedure based on the filtering length-scale $\bar{\Delta}$ (8), and \mathbb{T} as the same tensor however evaluated with an analytical filtering procedure based on a wider filtering length scale $\widehat{\Delta} > \bar{\Delta}$, we write:

$$\tau - \frac{1}{3} tr(\tau) \mathbb{I} = C_d \mathcal{F}(\bar{\Delta}, \bar{\rho}, \widehat{\mathbf{v}}); \quad (13)$$

$$\mathbb{T} - \frac{1}{3} tr(\mathbb{T}) \mathbb{I} = C_d \mathcal{F}(\widehat{\Delta}, \widehat{\rho}, \widehat{\mathbf{v}}); \quad (14)$$

where the anisotropic tensor \mathcal{F} stands for the chosen subgrid model which here is the vorticity model:

$$\mathcal{F}(\Delta, \rho, \mathbf{u}) = \mu_{sg} \left(\nabla \mathbf{u} + \nabla^t \mathbf{u} - \frac{2}{3} \nabla \cdot \mathbf{u} \mathbb{I} \right),$$

with the subgrid viscosity provided by Mansour et al. (1978):

$$\mu_{sg} = (\rho \Delta^2 \|\omega\|).$$

Here, C_d corresponds to the parameter of the model that must be adjusted following a dynamical procedure. Let us mention that without the dynamical procedure, C_d must hopefully converge toward the square of the vorticity model constant ($C_d = C_\omega^2$, with $C_\omega \in [0.1, 0.12]$, see relation (11)).

The relationship between τ and \mathbb{T} involves the Leonard's tensor (noted \mathbf{L}) that can easily be evaluated without any assumption since it is only based on resolved quantities:

$$\mathbb{T} - \widehat{\tau} = \mathbf{L} = \left(\widehat{\rho \widehat{\mathbf{v}} \otimes \widehat{\mathbf{v}}} - \widehat{\rho} \widehat{\widehat{\mathbf{v}}} \otimes \widehat{\widehat{\mathbf{v}}} \right). \quad (15)$$

The parameter C_d is then determined by minimizing the L^2 -norm of the modeling error through a Least-Square procedure (Lilly, 1992), assuming that C_d slowly evolves in space:

$$C_d = \left[\left(\mathbf{L} - \frac{1}{3} tr(\mathbf{L}) \mathbb{I} \right) : \mathbf{M} \right] \cdot [\mathbf{M} : \mathbf{M}]^{-1}. \quad (16)$$

\mathbf{M} is a tensor calculated by evaluating \mathcal{F} at two different cut-off wave numbers in (13) and (14):

$$\mathbf{M} = -C_d [\mathcal{F}(\widehat{\Delta}, \widehat{\rho}, \widehat{\mathbf{v}}) - \mathcal{F}(\bar{\Delta}, \bar{\rho}, \widehat{\mathbf{v}})]. \quad (17)$$

C_d (16) is evaluated at each point of the domain and at each time step. Let us remark that, in regions where the velocity gra-

dient of the macroscopic velocity is very low, high values of C_d can be recorded because the modulus of \mathbf{M} approaches zero. These values are not corrected as far as positive values are calculated since the parameter C_d , in the modeling of the subgrid stress tensor, is multiplied by the velocity gradient which gives rather low subgrid contributions. Nevertheless, negative C_d values can also be calculated and relatively large negative C_d values introduce anti-diffusive contribution that may lead to unstable computation. For this reason, as it is generally done in LES computations, we clip the C_d parameter to avoid negative C_d value and force $C_d = 0$ when negative values are calculated.

2.1.2. Model of the subgrid heat flux

A classic Fourier's law is used to express the subgrid heat flux as a product of the subgrid thermal conductivity and the first gradient of the resolved temperature. As far as the flow is isothermal, the dynamic procedure is not followed to evaluate the subgrid thermal conductivity in order to save computational time. Then, following the Reynolds analogy assumption, the subgrid thermal conductivity can be evaluated from the subgrid viscosity, similarly than the molecular thermal conductivity by using a constant subgrid Prandtl number assumption (Comte and Lesieur, 1998): $Pr_{sg} = 0.6$. The subgrid heat flux is then given by:

$$\psi = - \frac{\mu_{sg}}{(\gamma - 1) Re Pr_{sg} M_0^2} \nabla \tilde{T}. \quad (18)$$

3. Numerical approach

The resolution of the filtered Navier–Stokes Eqs. (1) and (2) has been performed by means of a finite volume approach. LES computations must use numerical schemes that can represent small scale structures with a minimum of numerical dissipation to minimize the interactions with the sub-grid scale modeling.

In the present study, the Euler part of the equations is discretized by means of a high-order coupled time and space scheme, named OS7 scheme, we developed in Daru and Tenaud (2004) based on a Lax–Wendroff approach, which ensures a high-order accuracy in both time and space. Detailed information on the development of this scheme and its implementation can be found in Daru and Tenaud (2004, 2009). The capabilities and the behavior of the OS7 scheme have already been studied on several relevant test cases, including those with large unsteady detachments. It was shown that, the time-space coupled OS7 scheme gives accurate results which compare very well with high order semi discrete procedures (methods of line), such as Runge–Kutta/WENO approaches, at a much lower computational cost. In Daru and Tenaud (2004), it was also demonstrated that the OS7 scheme achieves a very low level of error on coarse grids and, instead of a high-order WENO procedure, it should preferably be used in cases where it is not possible to use very fine meshes, which is a very standard situation for example in LES calculations where all the length scales are not fully resolved. Regarding the integration of diffusive fluxes, their integration can also be ensured by a coupled time-space procedure. The influence of the viscous flux discretization order on the solution of wall bounded flows at moderate Reynolds numbers were also performed in Daru and Tenaud (2009) where some simulations were conducted by using both 2nd- and 4th-order accurate centered schemes. It was found that (between 2nd- and 4th-orders) the order of the viscous scheme has negligible influence on the presented solutions of wall bounded flows at moderate Reynolds numbers. This is why in the present study, the space discretization of the diffusive fluxes is then obtained by means of a classical centered second-order scheme giving at last a second order accurate scheme in both time and space.

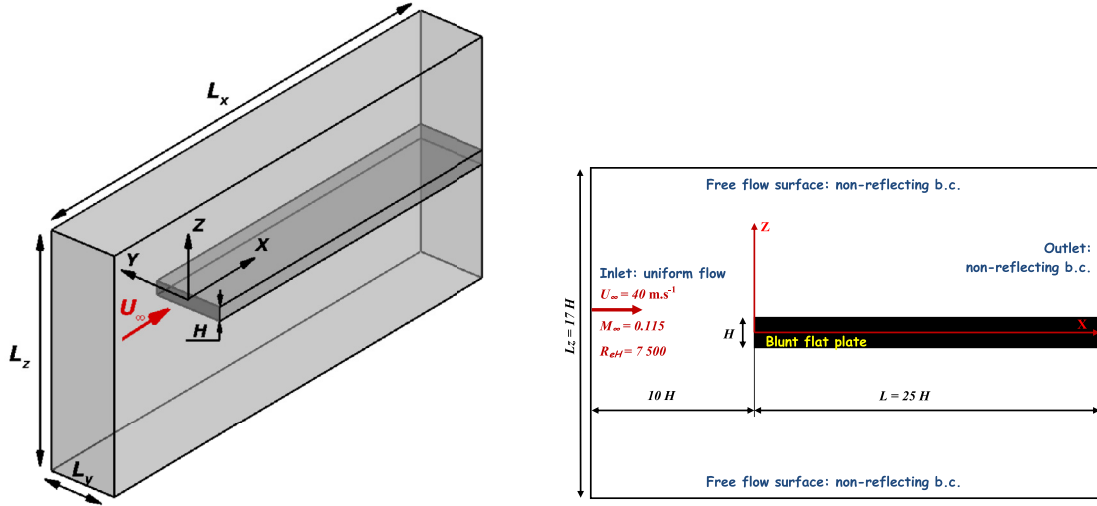


Fig. 1. Sketch of the computational domain around the flat plate (at the left) and prescribed boundary conditions (at the right).

4. Numerical procedure

4.1. Computational domain and boundary conditions

We consider an adiabatic blunt flat plate having a thickness H (taken as a reference length scale), mounted parallel to the free stream. It is equipped with a right-angled corner leading-edge. This flat plate spans the computational domain horizontally in its centerline, as seen in Fig. (1). The inlet boundary is located $10H$ upstream of the sharp leading edge to minimize its influence on the uniform inlet boundary condition. The flat plate has a streamwise length of $25H$, extending up to the streamwise outlet boundary. Simulations, that are not reported here for clarity, were previously performed on several domain dimensions to check the influence of the domain extents on the LES results. The influence of the width of the domain, associated to the spanwise homogeneous direction, the streamwise extent as well as the normal to the wall dimension were reviewed and no significant influence was recorded on mean and fluctuating quantities. Therefore, the computational domain sizes we retained to analyze LES results are $L_x = 35H$ in the streamwise direction, $L_y = 5H$ in the spanwise direction and $L_z = 17H$ in the normal to the flat plate direction. These domain sizes provide with blockage ratio that are equivalent to previous studies (Lamballais et al., 2010; Langari and Yang, 2013; Tafti and Vanka, 1991; Yang and Abdalla, 2009). These dimensions are required to largely weaken the influence of the domain boundaries. At the upstream boundary, a uniform flow is prescribed (ρ_∞ , U_∞ and T_∞) leading to the previous defined Mach ($Ma = 0.115$) and Reynolds ($Re_H = 7500$) numbers. As spanwise homogeneity is recovered in many experiments, for instance Kiya and Sasaki (1983) recovered flow uniformity over $\pm 3.5H$ on both sides of the midspan, periodicity is considered in the spanwise direction to study the intrinsic flow behavior without lateral wall-border effect. At the outlet as well as on upper and lower boundaries, non-reflecting conditions are prescribed by using characteristics based conditions (Poinsot and Lele, 1992).

4.2. Grid generation

A mesh refinement study has been undertaken to check its influence on statistical results. The mesh that gives rather grid independent results, consists in $(N_x \times N_y \times N_z) = (269 \times 121 \times 225)$ grid cells along the streamwise, spanwise and normal to the wall directions. Uniformly distributed grid points are used in the span-

wise direction with a grid spacing of $\delta y^+ = 16.6$, in terms of wall units. Wall units are calculated with respect to the friction velocity measured in the reattached boundary layer at $x/L_R = 3$; the friction velocity is almost constant further downstream. To well capture the flow dynamics, the grid was built with a lot of care, specially in the detached/reattached area, by using non-uniform grids in the streamwise (x) and the normal to the wall (z) directions. The mesh is then tightened in the normal to the wall direction to ensure a first cell size above the wall less than one wall unit ($\Delta z^+ = 0.94$). It is also tightened in the shear layer region edging the separation bubble. Distribution of space steps in wall units as well as grid spacing ratio between two consecutive cells are shown on Fig. 2 in the separated/reattached region. Let us emphasize that about 60 grid points in the normal to the wall direction are embedded in the reattached boundary layer. In the streamwise direction, grid is refined both at the leading edge and in the reattachment region ($2.4 \leq \delta x^+ \leq 24$). To judge refinements and stretchings of the mesh over the separated/reattached region, grid spacings in wall units and grid spacing ratios are given on Fig. 3 in the streamwise direction.

Though the mesh is stretched in the x - and z - directions, the grid spacing ratio between two consecutive cells is kept at low values over the separated/reattached region. The mesh used here is at least as refined as the one used in the study of Langari and Yang (2013) (and somewhere probably more refined).

4.3. Numerical implementation

Simulations were performed on a parallel / vectorial supercomputer (NEC - SX8) at IDRIS, the CNRS's national supercomputing center. As our LES software is based on explicit time and space integrations, a trivial domain decomposition by means of the MPI protocol, is adopted to decrease the restitution time. The computational domain is split into eight sub-domains having $135 \times 61 \times 113$ grid points each. The OS7 stencil spreading over nine grid points, sub-domains are overlapped over five grid points in each direction. On other words, quantities on five planes are exchanged per direction through the border between two consecutive sub-domains.

5. Numerical results

We consider an adiabatic blunt flat plate mounted parallel to a free stream and equipped with a right-angled leading-edge. The

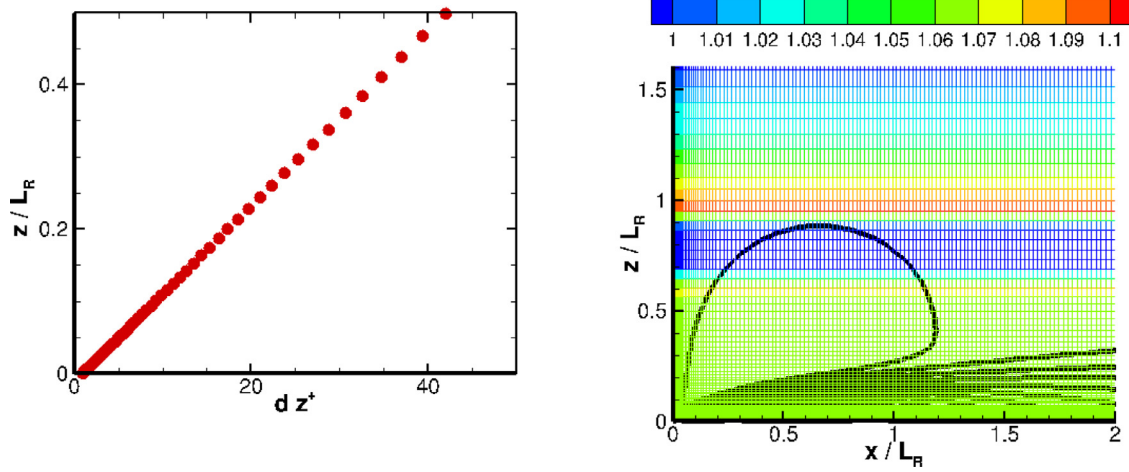


Fig. 2. On the left, grid spacing in wall units (δz^+) in the normal to the wall direction. On the right, mesh is colored with the ratio values of grid spacings between two consecutive cells. Isocountours of the mean streamwise velocity component are also superimposed on the mesh.

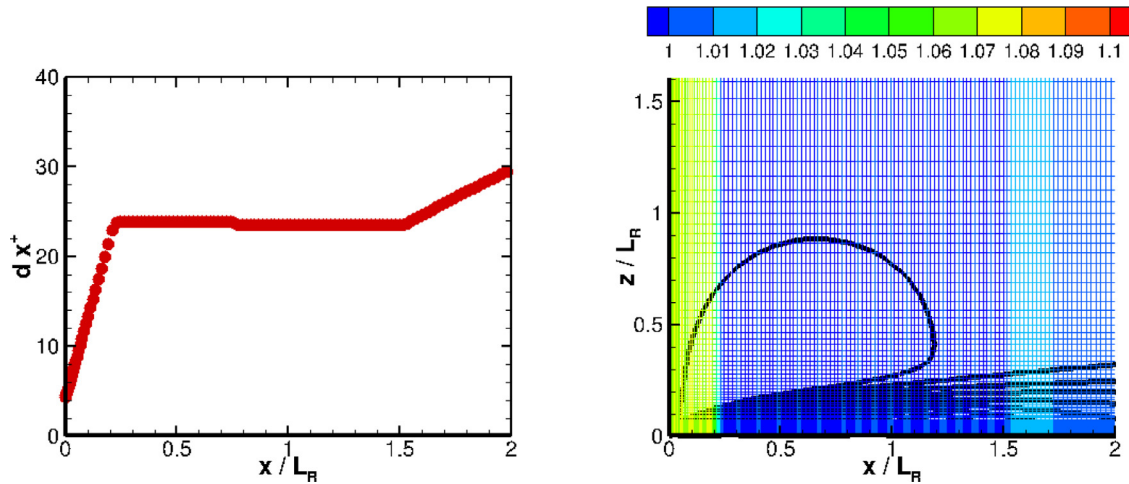


Fig. 3. On the left, Distribution of δx^+ in the streamwise direction. On the right, mesh is colored with the ratio values of grid spacings between two consecutive cells in the streamwise direction. Isocountours of the mean streamwise velocity component are also superimposed on the mesh.

plate thickness (H) and the uniform inlet velocity (U_∞) are taken as the main reference scales of the flow. The Mach number is prescribed at the value recorded in the Pprime Institute experiments at $Ma = 0.115$. To handle tractable *LES* regarding the CPU time consumption, the Reynolds number has been chosen ten times smaller than in the Pprime experiments (Sicot et al., 2012). Based on H , U_∞ , the density (ρ_∞) and the viscosity (μ_∞) evaluated at infinity, the Reynolds number is: $Re_H = 7500$. Note that this value is four to ten times smaller than experimental values found in the literature (Castro and Epik, 1998; Cherry et al., 1984; Kiya and Sasaki, 1983; 1985).

Fig. 4 presents an instantaneous field of the Q criterion (Jeong and Hussain, 1995) around the blunt flat plate. Isosurfaces of Q are colored with the velocity magnitude. This snapshot clearly illustrates the highly 3D feature of the flow structures in the vicinity of the blunt flat plate leading-edge. The sharp corner at the leading edge fixes the detachment location. Boundary layer separation then occurs over a large extent. The upper part of the separation bubble is bounded by a spatially developing mixing layer whose initial stage is certainly laminar and is followed by a breakdown toward turbulence through Kelvin–Helmholtz instability modes and roll pairing (see on Fig. 4 main rolls downstream the leading edge at edge of the recirculation for an illustration). Downstream a stable mixing layer at the leading edge, large scale structures, namely

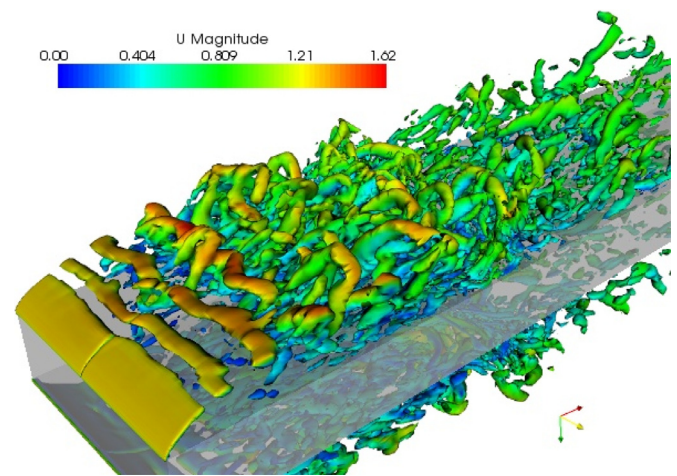


Fig. 4. Snapshot of an isosurface of the Q criterion ($Q = 3$) colored with the norm of the velocity in the vicinity of the plate leading-edge.

Kelvin–Helmholtz rolls, develop and break down to lambda-shape like patterns, further downstream. The flow behavior within the mixing layer development is mainly responsible for the separa-

tion extent (Castro and Epik, 1998). According to numerous experimental works (Castro and Epik, 1998; Cherry et al., 1984; Kiya and Sasaki, 1983; 1985), separation extent is about $L_R = 5H$. Several flow parameters such as the tunnel blockage, spanwise end-walls and the spanwise aspect ratio, free stream turbulence intensity, for instance, undoubtedly influence the mixing layer development and consequently the L_R value (Castro and Epik, 1998; Cherry et al., 1984; Hancock and Castro, 1993). When the mixing layer impacts the plate surface, a turbulent boundary layer develops further downstream. Structures within the upper part of the distorted boundary layer are elongated in the streamwise direction, influenced by the re-acceleration downstream the reattachment (Fig. 4). Two main unsteadinesses associated with the separation are generally educed: the shedding and the flapping modes. The former is relative to the vortex shedding and is associated with the usual large scale motions of the shear layer. The latter, the low-frequency flapping mode, is an overall dynamical mechanism linked to successive enlargements and shrinkages of the separated zone.

It was largely demonstrated that the free-stream turbulence has an influence on some flow characteristics. In fact, free stream turbulence influence the transition in the mixing layer (Cherry et al., 1984). The turbulence seems to be earlier tripped in the mixing layer, inducing earlier reattachment than without free-stream turbulence (Hillier and Cherry, 1981; Saathoff and Melbourne, 1997; Yang et al., 1999). Nevertheless as the first step in this study, we decided to not consider the free-stream turbulence as inlet perturbations to decouple the influence of several parameters, unlike Langari and Yang (2013) and Yang and Abdalla (2009). We will however see hereafter that taking the separation length as the reference length scale, the present *LES* results obtained without free-stream turbulence, compare very well with experiments. Influences of free-stream turbulence are not the purpose of this paper and could be studied numerically in the near future.

We first validated *LES* results obtained through the use of the mixed-scale model. We then studied the influence of the subgrid-scale model by comparing first results to those obtained by means of the dynamical vorticity model. We finally analyzed the space and time dynamics of the flow in the vicinity of the leading edge.

For comparisons we need to evaluate mean quantities (noted $\langle \bullet \rangle$) that are calculated by using integrations in both time and spanwise (homogeneous) direction: $\langle \bullet \rangle = \frac{1}{L_y T} \int_{L_y} \int_T \bullet dt dy$, where T is the integration period. Dimensionless times are estimated by means of the inlet velocity (U_∞) and the plate thickness (H). Mean quantities are computed as soon as a statistically converged state is reached. This convergence is checked on the time evolution of the L^1 -, L^2 - and L^∞ -norms of both the mean and *r.m.s.* values of the velocity components and the pressure. We assumed that it was reached for a dimensionless time of about $t_0 = 110$. Statistical quantities are then calculated from t_0 and recorded over a dimensionless time interval $\Delta t = 340$, approximately corresponding to forty vortex shedding events.

5.1. Validation of *LES* results

In this section, *LES* results are obtained by means of two subgrid-scale models: the compressible version of the mixed-scale model (Section 1.1.1.1) and the well known dynamical procedure (Germano et al., 1991) applied to a classical vorticity model (Mansour et al., 1978) (Section 1.1.1.2). Although the numerical scheme is deliberately high order accurate to minimize both the dissipative and the dispersive errors, while very weak it however has a dissipative-diffusive interaction with the diffusive subgrid-scale model. It is then mandatory to employ different subgrid-scale models to measure their influence on *LES* results. Both results are compared either to the Pprime experiments (Sicot et al., 2012) or to results from the literature.

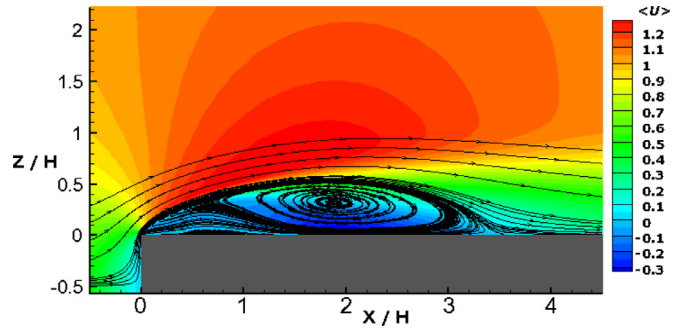


Fig. 5. Streamlines superimposed onto the isocountours of the streamwise velocity component ($\langle U \rangle$), in the upper region close to the leading edge: *LES* results obtained with the mixed-scale model.

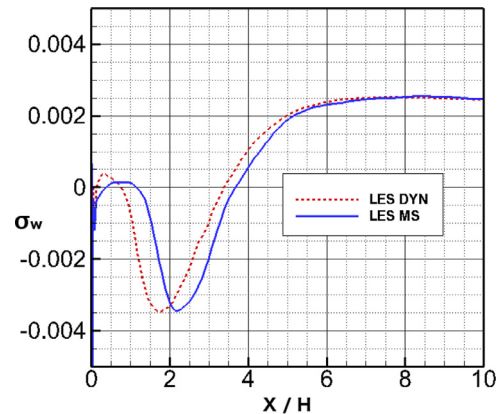


Fig. 6. Streamwise distribution, at the upper wall of the blunt flat plate, of the mean shear stress predicted by the *LES* through the mixed-scale model (—) and the dynamic vorticity model (- - -).

Fig. 5 shows streamlines of the mean flow predicted by *LES* with the mixed-scale model, which are superimposed onto iso-countours of the streamwise velocity component ($\langle U \rangle$). The thickness of the main clockwise bubble is estimated at $z_R/H = 0.53$ (corresponding to $z_R/L_R = 0.14$, for direct comparison with (Tafti and Vanka, 1991), where L_R is the reattachment length). A secondary mean anti-clockwise vortex is clearly visible very close to the leading-edge for which its streamwise location is $x_{R_2}/H \in [0.355, 1.16]$ ($x_{R_2}/L_R \in [0.1, 0.315]$) and its thickness is $z_{R_2}/H = 0.048$ ($z_{R_2}/L_R = 0.013$). These reverse flow contours are in a good agreement with those obtained through the DNS results of Tafti and Vanka (1991) at however a lower Reynolds number ($Re_H = 1\ 000$).

The spanwise averaged value of the reattachment length constitutes the first characteristic quantity of the separation. It is generally defined as the distance from the leading-edge where the average (in time and spanwise direction) value of the wall shear stress reaches zero. Fig. 6 shows the streamwise distribution of the mean shear stress predicted along the upper wall of the blunt flat plate. The L_R value predicted by using the mixed-scale model is $L_R/H = 3.68$. The reattachment length is however slightly lowered by the dynamic vorticity model since $L_R/H = 3.38$. Present predictions underestimate the generally admitted experimental mean reattachment length since the value across the literature is $L_R/H = 5$ (Cherry et al., 1984), at high Reynolds number flows. This specific value has clearly been recovered in the Pprime experiments (Sicot et al., 2012). However, at high Reynolds number regime, all experimental studies did not recover a unique value since L_R/H is distributed in between $[4, 5.5]$ (see Cherry et al., 1984). Following pre-

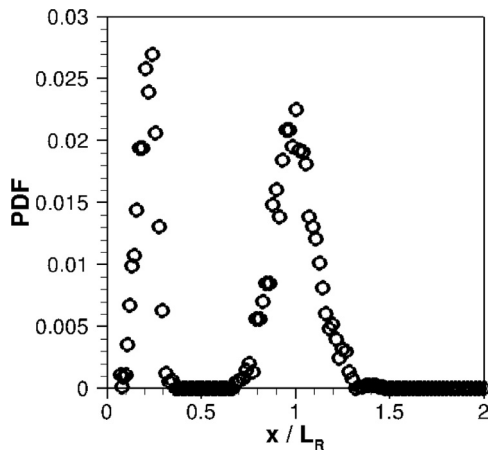


Fig. 7. Probability density function of $\frac{\partial u}{\partial x} = 0$ along the upper wall of the blunt flat plate, predicted by the LES with the dynamic vorticity model.

vious numerical studies at low and moderate Reynolds numbers, values found for the reattachment length are clearly dispersed. At low Reynolds numbers, much greater values than the one generally admitted are recorded: Tafti and Vanka (1991) obtained $L_R/H = 6.36$ at $Re_H = 1\,000$ while Lamballais et al. (2010) obtained values close to $L_R/H = 7$ at $Re_H = 2\,000$ whatever the radius of the rounded leading edge is. Transition delay in the mixing layer might explain these large L_R values. At moderate Reynolds number ($Re_H = 3\,450$, Yang and Voke (2000); 2001) recovered a smaller value ($L_R/H = 2.58$). Besides, Ji and Wang (2010) recorded a reattachment length that is close to 3 in a forward facing step configuration at $Re_H = 21\,000$. The present L_R value is rather close to the lower bound of the experimental values. It is however clearly consistent with values recorded by other numerical studies at moderate Reynolds numbers (Ji and Wang, 2010; Yang and Voke, 2000; 2001). More recently, a benchmark study (Bruno et al., 2014) on the aerodynamics of rectangular cylinders was published providing numerous results either experimental or numerical, on the blunt flat plate configuration at several moderate to high Reynolds numbers. It was reported that a significant variability of the separation length was recorded without easily identifying a trend with the different simulation parameters. It is then obvious that addi-

tional investigations must be undertaken to understand the reason of such dispersed L_R values.

As pointed out by Yang and Voke (2000), the reattachment length largely varies in time. This behavior is exhibited in Fig. 7 where the probability density function of zero wall shear stress is plotted versus the streamwise location. Regarding the main clockwise vortex, the PDF is symmetrically distributed around the mean reattachment location. However, amplitudes of the reattachment length fluctuations are really important since L_R varies from 60% of the mean reattachment length ($L_R \in [0.7, 1.3]$). Regarding the secondary anti-clockwise vortex, the PDF distribution suggests that it could completely disappear from time to time.

To compare with exiting results of the literature, altitudes of both the center (z_c) and the edge (z_δ) of the mixing layer bounding the upper part of the separation, are plotted versus the streamwise distance from the leading-edge (Fig. 8). Definitions of z_c and z_δ are the ones used by Tafti and Vanka in their DNS study (Tafti and Vanka, 1991). In fact, z_c is the altitude where u_{rms} reaches its maximum value. Following the early experimental studies of Djilali and Gartshore (1991) and Cherry et al. (1984) (see Tafti and Vanka, 1991), the altitude (z_δ) of the mixing layer edge is defined as the location where $u_{rms}/U_\infty = 2.5\%$. Present LES predictions of z_c compare very well with values estimated from both the Pprime experiments (Sicot et al., 2012) (Fig. 8, left) and the experimental results from Kiya and Sasaki (1983) (that have been recorded from Tafti and Vanka, 1991) (Fig. 8, right). Since LES predictions with both subgrid-scale models on z_c rather collapse, the subgrid-scale model does not affect very much the location where u_{rms} is maximum as we will see hereafter on the mean turbulence quantity profiles (Fig. 12, for instance). More variability is noticeable on the altitude of the mixing layer edge (z_δ) (Fig. 8). The subgrid-scale model seems to have an influence of the edge position of the mixing layer. As we can see in the followings, the more diffusive the model, the thicker the mixing layer. The predictions obtained by means of the mixed-scale model better agree with experimental values of Kiya and Sasaki (1983) and the DNS values from Tafti and Vanka (1991) while those predicted by using the dynamic vorticity model are more in accordance with the Pprime experiments (Sicot et al., 2012). However, we must add that, as PIV measurements in the Pprime experiments (Sicot et al., 2012) recorded high intensities of the free stream turbulence in the most downstream PIV window (see Fig. 12), it is delicate to extract the edge location.

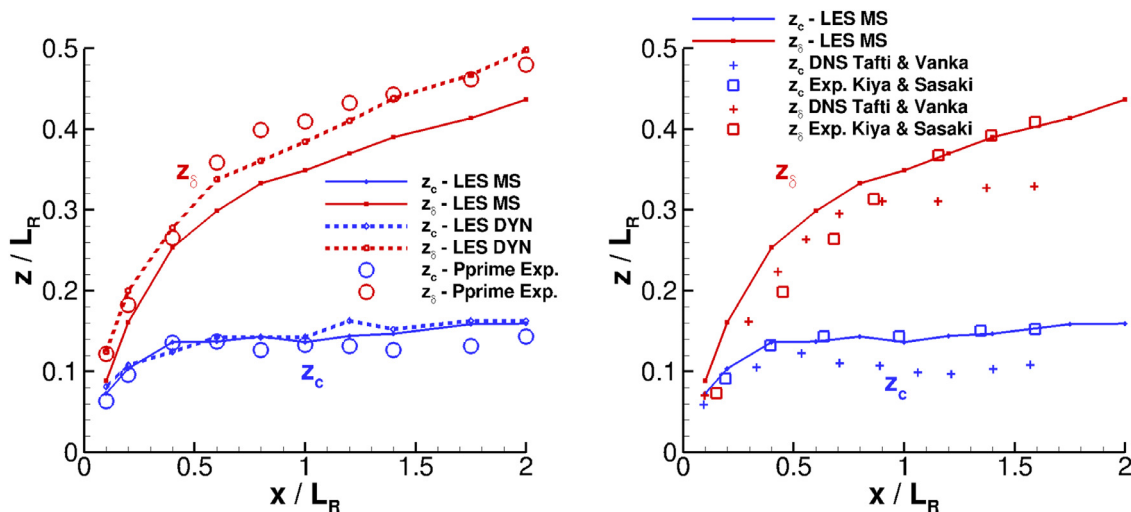


Fig. 8. Distributions of the altitudes of both the center (z_c) and the edge (z_δ) of the mixing layer: on the left, present LES results obtained with either the mixed-scale model (—) or the dynamic vorticity model (- - -), compared to the Pprime experiments (Sicot et al., 2012) at $Re_H = 80\,000$ and, on the right, present LES results with mixed scale model compared to the experiments from Kiya & Sasaki (recorded from Tafti and Vanka, 1991), at $Re_H = 26\,000$, and the DNS results from Tafti and Vanka (1991), at $Re_H = 1\,000$.

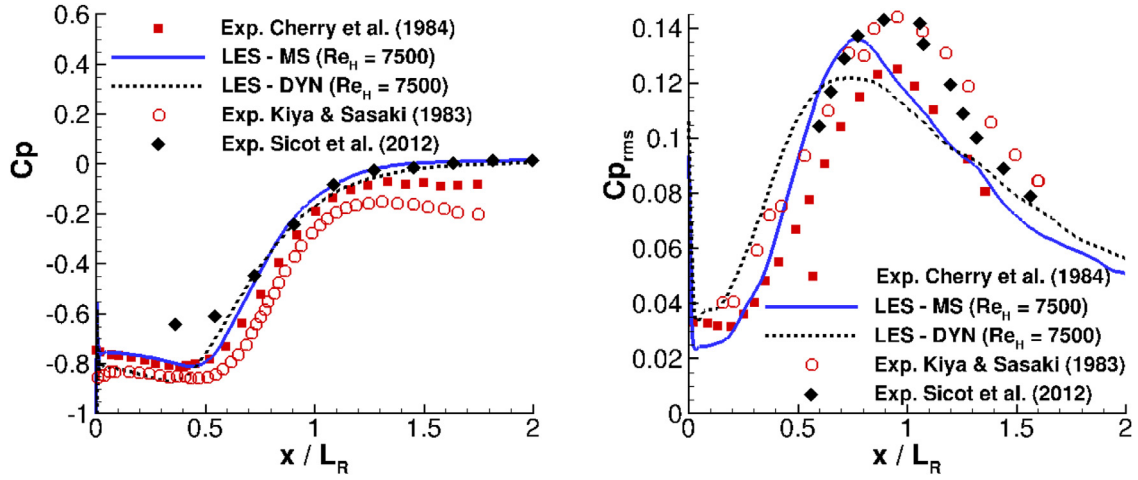


Fig. 9. Streamwise wall pressure distributions obtained by *LES* either with the mixed-scales model (—) or with the dynamic vorticity model (- - -), compared to experiments from [Cherry et al. \(1984\)](#) (red plained square), [Kiya and Sasaki \(1983\)](#) (red opened circle) and [Sicot et al. \(2012\)](#) (black plained diamond), on both the mean (left) and the fluctuating (right) pressure coefficients. (For interpretation of the references to colour in this figure legend, the reader is referred to the web version of this article.)

Therefore, we only estimate the value of z_δ from Pprime experiments ([Sicot et al., 2012](#)). Though some discrepancies are noticeable in the *LES* predictions, the slope of z_δ , mainly for the most downstream locations, agrees fairly well with experimental ones whatever the model is, in the contrary of the DNS of [Tafti and Vanka \(1991\)](#).

LES results on velocity and pressure, for instance, can be compared with different data obtained at several Reynolds numbers, when quantities made dimensionless by using reference values at infinity, are plotted versus dimensionless coordinates using L_R as reference length. [Fig. 9](#) shows the predicted streamwise distribution of the wall mean pressure coefficient ($C_p = 2 \cdot \frac{\langle P \rangle_{wall} - P_\infty}{\rho_\infty U_\infty^2}$) and its *rms* value ($C_{p_{rms}} = 2 \cdot \frac{\sqrt{\langle p'^2 \rangle}}{\rho_\infty U_\infty^2}$), both compared to the experimental results of [Cherry et al. \(1984\)](#). Regarding the *LES* results, the predicted general trend of the C_p distribution for both subgrid models fit very well the experiments. The abrupt C_p increase has to be related to the mean flow deceleration in the longitudinal direction, upstream of the reattachment. The *LES* results predict correctly the location from where the pressure rise occurs and correctly foresee this deceleration. Downstream the reattachment, the *LES* roughly recovers the mean pressure value at infinity, that however overpredicts the experimental values. Discrepancies on C_p between both subgrid models are not significative and are of the same order of differences between experiments. Though some discrepancies are noticeable on the streamwise distribution of $C_{p_{rms}}$, the general trend of experimental data is recovered by the present *LES* results. The magnitude of the $C_{p_{rms}}$ peak is rather well predicted since its value is in between experimental measurements of [Kiya and Sasaki \(1983\)](#); [Sicot et al. \(2012\)](#) ($C_{p_{rms}} \# 0.145$) and [Cherry et al. \(1984\)](#) ($C_{p_{rms}} \# 0.125$) ([Fig. 9](#)). *LES* with the mixed-scale model predicts the $C_{p_{rms}}$ peak magnitude of 0.138 at a location $x/L_R = 0.79$ which are in very good agreement with the values obtained by [Tafti and Vanka \(1991\)](#) through a DNS approach (see [fig. 12 of Tafti and Vanka, 1991](#)).

[Figs. 10 and 11](#) compare to the Pprime measurements ([Sicot et al., 2012](#)), the streamwise ($\langle U \rangle$) and the wall-normal ($\langle W \rangle$) components of the mean velocity obtained by the present *LES* at several streamwise locations ($x/L_R = 0.2, 0.4, 0.8, 1., 1.5, 2.$). From a general point of view, predicted and measured mean velocity profiles are in a fairly good agreement though the Reynolds number in the computations is much lower than in the experiments. No significant discrepancies on the mean velocity profiles

are recorded between the two subgrid models. Note that profiles of the wall-normal mean velocity are generally not shown in papers because large discrepancies are often recorded between experiments and simulations. Here, they fit very well experiments. Let us mention that very close to the wall, a few strange experimental values were recorded, mainly on the wall-normal component of the mean velocity. Following a private communication with Poitiers experimentalists, these “spurious” values must certainly be attributed to laser-light reflection on the flat plate surface. Although the center of the mixing layer is rather well predicted as mentioned above, *LES* results exhibit small discrepancies that must be analyzed, when they are compared to experimental profiles. At the first locations (*i.e.* $x/L_R = 0.2$ and 0.4), the streamwise mean velocity is slightly overestimated in the outer flow. This might be attributed to a too important longitudinal velocity gradient induced by an effect of solid blockage ratio ($1/16$ in the wall-normal direction, in the computations) which is greater than in the experiments, although non reflecting boundary conditions are applied on the upper and the lower boundaries. Further downstream, the external mean velocity values rapidly recover the experimental values. Similar trends as the ones predicted here are also noticeable on mean streamwise velocity profiles coming from both the DNS of [Tafti and Vanka \(1991\)](#) and the *LES* of [Yang and Voke \(2001\)](#). Though discrepancies are here rather small, they might be attributed to a possibly low Reynolds number effect since the transition in the mixing layer is slightly postponed more downstream and the diffusion seems barely higher afterwards.

Comparisons on Reynolds stress component profiles between *LES* results and Pprime experiments ([Sicot et al., 2012](#)) are illustrated at several streamwise locations, in [Figs. 12–14](#). As mentioned above, we note that the location of the mixing layer is rather well predicted so that it is not necessary to redefine the vertical coordinate as [Tafti & Vanka](#) did in [Tafti and Vanka \(1991\)](#). Uncertainties of measurements are noticeable, mainly in the free stream where high turbulence intensity is recorded at several locations. free stream turbulence intensities seem very high in the experiments since Although PIV measurements ([Sicot et al., 2012](#)) recorded unusual high intensities of the free stream turbulence in the most downstream PIV window, under-predictions of both models in the free stream part of the flow must be attributed to lack of inlet perturbations to mimic free stream turbulence. However elsewhere in the flow, we can remark that the present *LES* gives good results which compare favorably with previous *LES* results

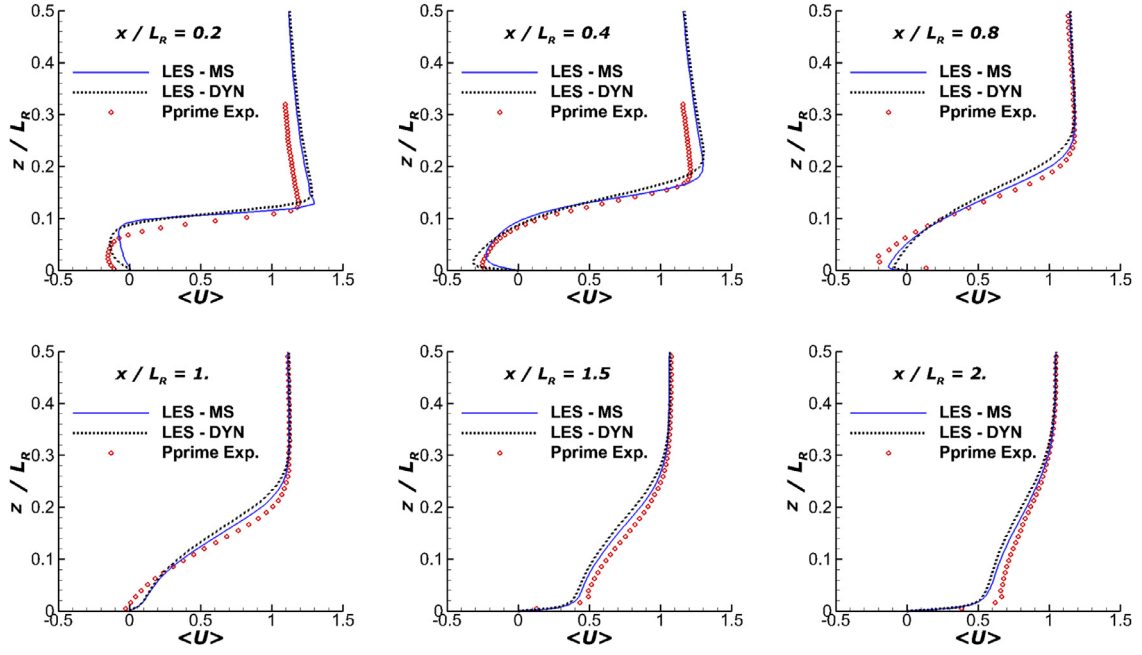


Fig. 10. Profiles in the wall-normal direction of the streamwise component of the mean velocity ($\langle U \rangle / U_\infty$): *LES* results with either the mixed-scale model (—) or the dynamic vorticity model (- - -), compared to Pprime experiments (Sicot et al., 2012) (●).

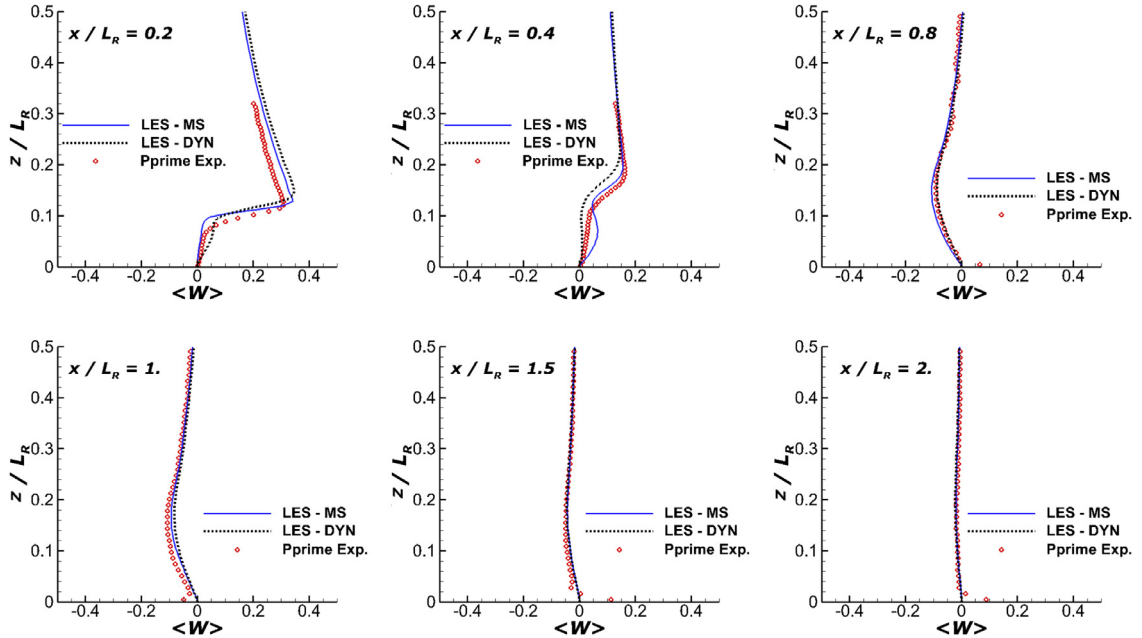


Fig. 11. Profiles in the wall-normal direction of the wall-normal component of the mean velocity ($\langle W \rangle / U_\infty$): *LES* results with either the mixed-scale model (—) or the dynamic vorticity model (- - -), compared to Pprime experiments (Sicot et al., 2012) (●).

(Langari and Yang, 2013; Tafti and Vanka, 1991; Yang and Voke, 2001). At the first location ($x/L_R = 0.2$) the dynamic vorticity model largely overpredicts turbulence intensities and the turbulent shear-stress. This must come from the vertical gradient of the mean streamwise velocity that is greater than the experimental one at this location (Fig. 10). The mixed-scale model agrees very well with experiments, especially on the vertical *rms* component (Fig. 13) and the turbulent shear-stress (Fig. 14), though the peak of the streamwise *rms* component within the mixing layer is barely under-predicted (Fig. 12). Further downstream, *LES* results obtained with both models agree rather well. Compared to Pprime experi-

ments (Sicot et al., 2012), *LES* overestimated turbulence intensities in the middle part of the detachment ($x/L_R = 0.6 - 0.8$). Further downstream, intensities of the Reynolds stress components are better estimated, though slight under-predictions are noticeable on the streamwise component (Fig. 12) and the cross-correlation (Fig. 14). The maximum magnitude of the *rms* and cross-correlation values occur close to ($x/L_R = 0.6 - 0.8$) which is somewhat more upstream than in the experiments since maxima are reached close to the reattachment ($x/L_R = 0.8 - 1$). Then, the mean turbulence intensities decrease further downstream, to recover classical turbulent boundary layer levels while the turbulent boundary layer is

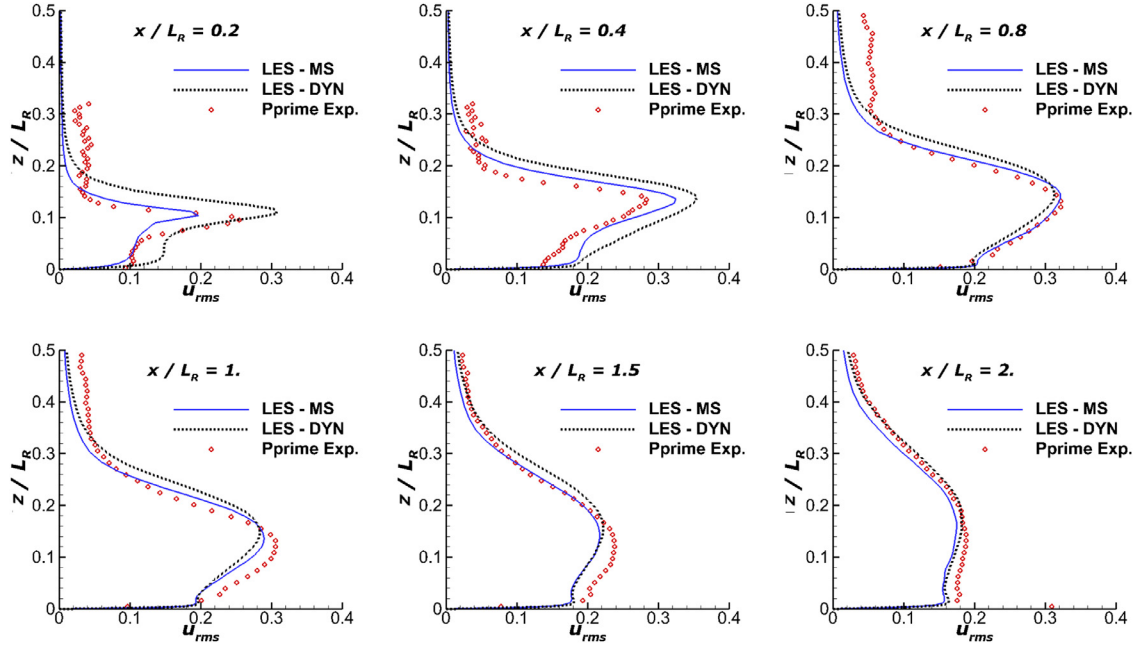


Fig. 12. Profiles in the wall-normal direction of the streamwise Reynolds stress ($\langle u'^2 \rangle^{1/2} / U_\infty$): LES results with either the mixed-scale model (—) or the dynamic vorticity model (- - -), compared to Pprime experiments (Sicot et al., 2012) (●).

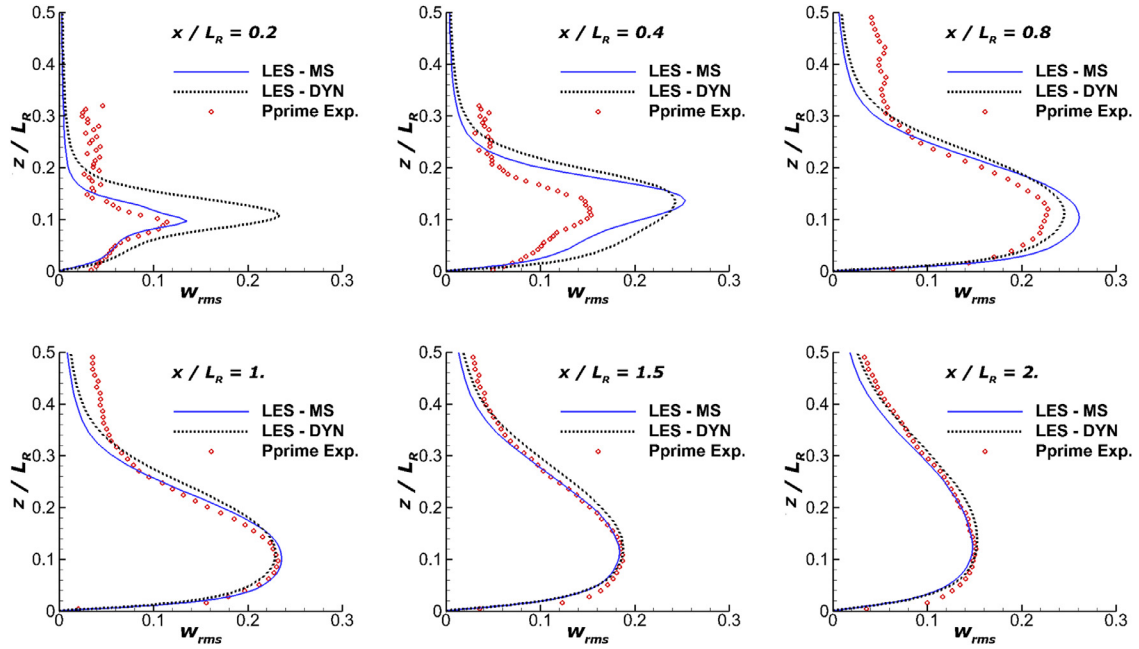


Fig. 13. Profiles in the wall-normal direction of the wall-normal Reynolds stress ($\langle w'^2 \rangle^{1/2} / U_\infty$): LES results with either the mixed-scale model (—) or the dynamic vorticity model (- - -), compared to Pprime experiments (Sicot et al., 2012) (●).

far away of reaching an equilibrium state. Let us remark that these considerations on streamwise locations and magnitudes of mean turbulent quantity maxima are quite consistent with the streamwise distribution of the *rms* pressure coefficient (Fig. 9).

To highlight the distortion occurring in the boundary layer detachment and just downstream, we plot the correlation coefficient between the streamwise and the vertical fluctuations (Fig. 15) which is almost constant in a standard turbulent boundary layer, reaching a value close to $\frac{-\langle u'w' \rangle}{(u_{rms} \cdot w_{rms})} = 0.45$. We also plot the ratio between the turbulent shear-stress and the turbulent kinetic energy ($\langle k \rangle = \frac{1}{2} (\langle u'^2 \rangle + \langle w'^2 \rangle + \langle v'^2 \rangle)$), which normally recovers an almost constant value $\frac{-\langle u'w' \rangle}{\langle k \rangle} = \sqrt{C_\mu} = 0.3$ following

classical constant value for standard turbulent boundary layer. Results obtained by means of the two subgrid-scale models rather agree with each other. However, some discrepancies are noticeable at the second location ($x/L_R = 0.4$) where peaks on $\frac{-\langle u'w' \rangle}{(u_{rms} \cdot w_{rms})}$ and $\frac{-\langle u'w' \rangle}{\langle k \rangle}$ are clearly visible within the mixing layer on results with the mixed-scale model while these quantities remain rather constant across the boundary layer with the dynamic vorticity model. This might suggest that the dynamics in the mixing layer occurs earlier than by using the mixed-scale model. This is also consistent with streamwise evolutions of both the mean quantity and the Reynolds stress profiles presented above. Across the detachment, maxima of ratios are situated within the mixing layer

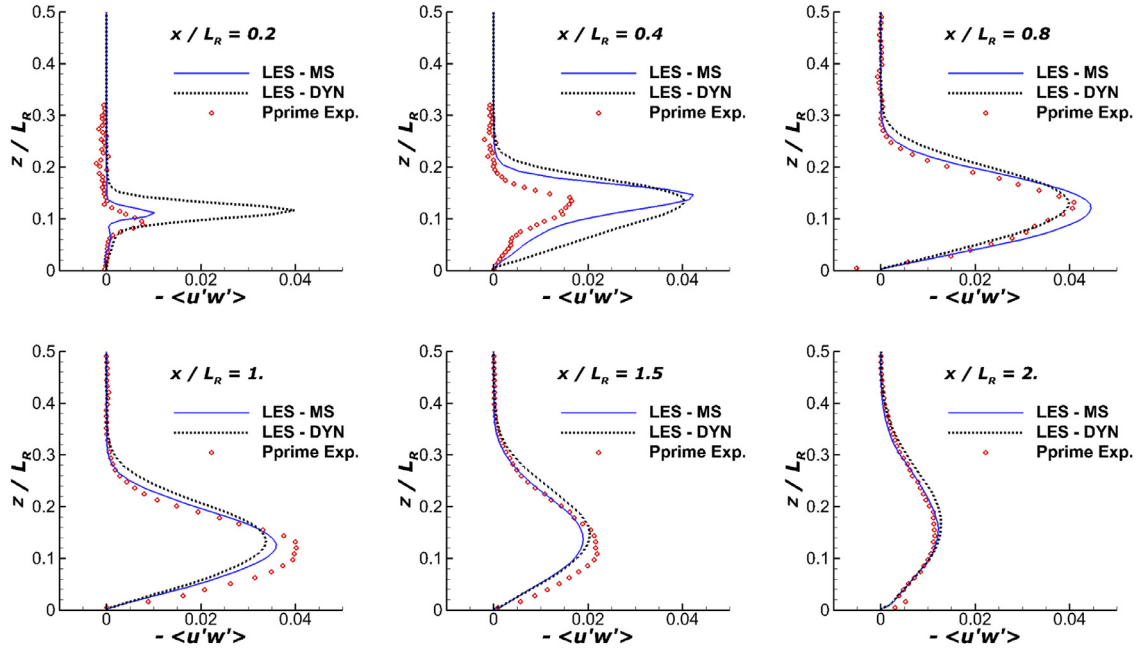


Fig. 14. Profiles in the wall-normal direction of turbulent shear-stress $-\langle u'w' \rangle / U_\infty^2$: LES results with either the mixed-scale model (—) or the dynamic vorticity model (- - -), compared to Pprime experiments (Sicot et al., 2012) (●).

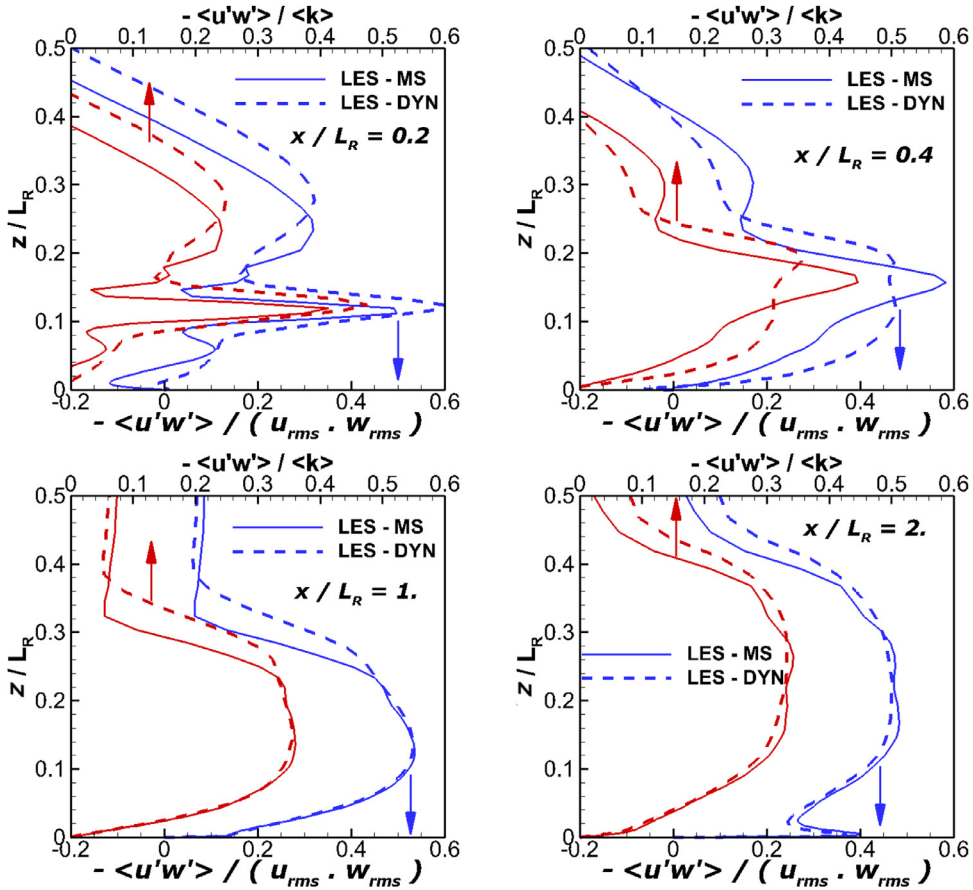


Fig. 15. Profiles in the wall-normal direction of the correlation coefficient $\frac{-\langle u'w' \rangle}{(u_{rms} \cdot w_{rms})}$ (bottom axis and blue lines) as well as the ratio $\frac{-\langle u'w' \rangle}{\langle k \rangle}$ (top axis and red lines): LES results are obtained with either the mixed-scale model (—) or the dynamic vorticity model (- - -). (For interpretation of the references to colour in this figure legend, the reader is referred to the web version of this article.)

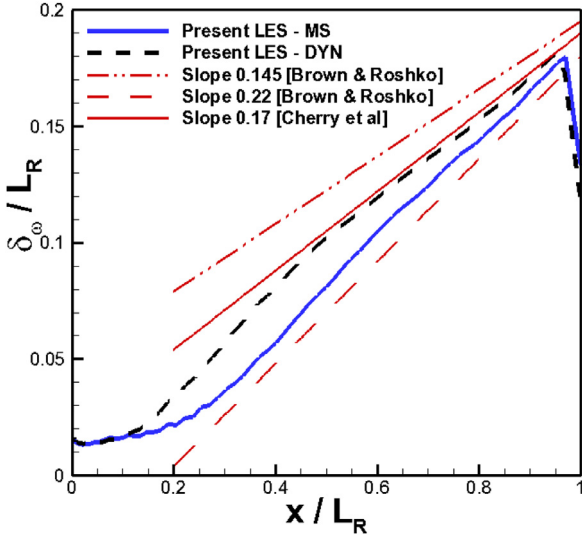


Fig. 16. Longitudinal distribution of the vorticity thickness (δ_ω) of the mixing layer edging the separation, obtained with the mixed-scale model (—) or the dynamic vorticity model (- - -). For comparison, classical values of the mixing layer expansion (Brown and Roshko, 1974; Cherry et al., 1984) are also reported.

exhibiting however rather high values compared to the standard values. At the reattachment location and further downstream, though high levels are recorded across the boundary layer, they decrease in the streamwise direction to reach values (i.e. $\frac{-\langle u'w' \rangle}{(u_{rms} \cdot w_{rms})} = 0.48$; $\frac{-\langle u'w' \rangle}{\langle k \rangle} = 0.33$) that are rather close to standard values at the most downstream location analyzed ($x/L_R = 2$).

Present LES results on the mean velocity as well as on the mean turbulent quantities show the same trends as those of both the DNS results of Tafti and Vanka (1991) (see fig. 8, 9, 10 and 14 of Tafti and Vanka, 1991) and the LES of Yang and Voke (2001) (see Fig. 3 of Yang and Voke, 2001). Similar conclusions were already mentioned by these authors on the discrepancies occurring on the mean turbulent quantities, pointing out that these discrepancies might come from a low Reynolds number effect.

It is well known that the mixing layer edging the separation mainly drives the dynamics of the flow in the separation region and even further downstream (Castro and Epik, 1998; Cherry et al., 1984; Yang and Voke, 2001). To be relevant, it is then mandatory that simulations correctly predict the main features of this mixing layer. As we saw before, the center and the edge of the mixing layer are rather well predicted by the present LES either with the mixed-scale model or the dynamic vorticity model. To better characterize the mixing layer, one of the common length scales generally used is the vorticity thickness (δ_ω), defined as follows:

$$\delta_\omega(x) = \frac{(\langle U \rangle_{\max_z} - \langle U \rangle_{\min_z})}{\max_z \left(\frac{\partial \langle U \rangle}{\partial z} \right)}. \text{ As it is well known (Brown and}$$

Roshko, 1974; Cherry et al., 1984), (δ_ω) must follow a linear evolution versus the main flow direction, as far as the mixing layer reaches an asymptotic behavior, i.e. downstream the first pairing of the Kelvin–Helmholtz rolls. The distribution of δ_ω along the main flow direction is presented in the Fig. 16 for both the mixed-scale model and the dynamic vorticity model. Streamwise evolutions of the mixing layer expansion for both subgrid models seem consistent with distribution of pressure coefficients (Fig. 9) and Reynolds stress profiles (Figs. 12–14). Expansions of the mixing layer predicted by the two subgrid models agree very well with the classical averaged slope value $\langle d\delta_\omega/dx \rangle = 0.17$ recovered by Cherry et al. (1984) through a collection of measurements resulting from the literature. Predicted δ_ω growth rates also agree very well with the upper bounds of expansion rate generally admitted for a single-

stream mixing layer (i.e. with effectively zero velocity on one side) which are in between 0.145 and 0.22 (Brown and Roshko, 1974).

6. Modal decomposition analysis

In all that follows, all quantities are nondimensionalized with the far-stream velocity U_∞ and the plate thickness H .

6.1. The POD technique

POD is a statistical technique (Holmes et al., 1996) which extracts the most energetic motions of the flow. Any physical quantity $q(\underline{x}, t)$ (which can be the velocity field, density, or any combination thereof) can be written as:

$$\underline{q}(\underline{x}, t) = \sum_{n \geq 1} (\lambda^n)^{1/2} a^n(t) \underline{\phi}_q^n(\underline{x}), \quad (19)$$

where $\underline{\phi}_q^n$ is the n th eigenvector of the time-averaged spatial auto-correlation tensor ($\langle q(\underline{x}, t) q(\underline{x}', t) \rangle$), λ^n represents the energy of the n th mode, and $a^n(t)$ is the temporal coefficient representing the amplitude of the n th mode.

A snapshot POD analysis (Sirovich, 1987) was applied to the full field $q = (\rho, \underline{v}, E)$ over the entire numerical domain as well as to its restriction to the volume above the plate. No renormalization was applied to the different physical variables, i.e. the density, the velocity and the total energy. It has been shown in the case of thermal convection (Podvin and Quéré, 2001) that rescaling had very little influence on POD results. Moreover, we checked that velocity modes obtained with the full field decomposition were similar to those obtained by considering only the velocity field, which is expected since the flow is nearly incompressible. We also performed POD analysis of the surface pressure field on one of the horizontal wall of the plate. In both cases the method of snapshots was used with 320 fields with a time separation of $0.08H/U_\infty$ time units.

6.2. Full-field POD

The full flow was included in the analysis and its time-average was found to be identical with the first POD mode. The POD energy λ^1 associated with the mean flow is much higher than the total fluctuating energy. As shown in Fig. 5, a quasi-2D vortex can be distinguished in the recirculation bubble for the mean flow. The characteristics of the main vortex were determined from examination of the flow streamlines. As mentioned earlier, the vertical extent of the main vortex is about $0.5H$, which is equal to the height of the recirculation bubble. Its longitudinal extent is smaller than that of the bubble ($2.5H$ against $3.38H$).

Fig. 17 shows the higher-order eigenvalues $n \geq 2$ when the POD was applied to the full field over the entire domain. We emphasize that the n -th most energetic fluctuation corresponds to the $n+1$ th mode. The POD spectrum of the 3D velocity fluctuations is presented in Fig. 17(a). No significant differences were observed when only the upper half-volume (flow above the plate) was considered. The spectrum of the surface pressure fluctuations (on the upper wall) is shown in Fig. 17(b). A blow-up of the spectrum for the largest modes is shown in the inset. The velocity spectrum decays relatively slowly: the 100th fluctuating velocity mode and an energy which is still 1/6 of the most energetic fluctuating mode, while in contrast that of the 100th pressure mode is less than 1/40 that of the most energetic pressure mode. The relatively slow decay of the velocity spectrum is evidence of the complexity of the

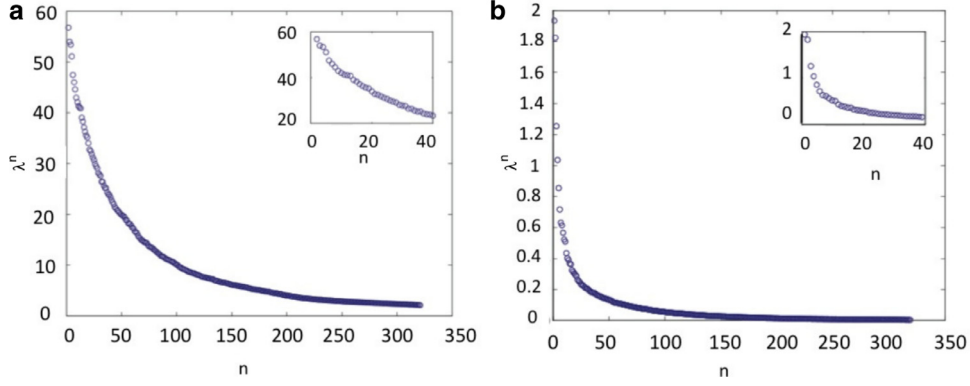


Fig. 17. (a) POD spectrum of the full field fluctuations ($n \geq 2$) (b) POD spectrum of the wall pressure fluctuations .

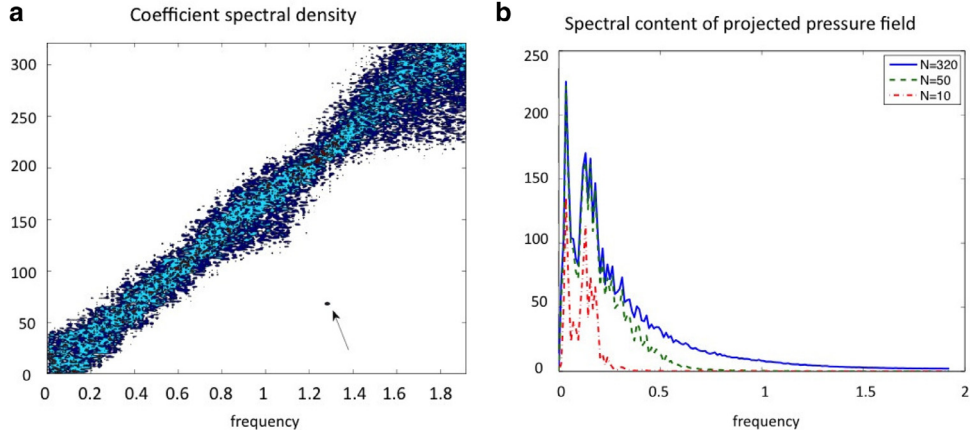


Fig. 18. The frequency is nondimensionalized with the plate thickness (a) spectral density of the pressure POD coefficients a_p^n . The arrow indicates the location of the Kelvin–Helmholtz frequency (b) spectral density of the POD energy $\sum_{n=2}^{N+1} \lambda^n |\hat{a}^n(f)|^2$.

flow. In contrast, the pressure field is relatively less complex, which can be expected from the fact that it is a scalar measured on a plane, while the velocity is 3D and obtained on the entire domain.

The temporal amplitudes of the POD spatial modes were computed and their Fourier transform is represented in Fig. 18. It shows that the POD organization of the flow consists of a superposition of modes associated with frequencies which increase with the order of the modes. The increase is essentially linear, which is reminiscent of wave-like structures. Fig. 18(a) shows that the 50 first modes of the velocity field are associated with low frequencies $fU/H_\infty \leq 0.2$.

Fig. 18 (b) indicates that four peaks can be clearly identified in the total spectrum – one at the frequency of $f_1H/U_\infty = 0.04 - 0.05$, another at a frequency of $f_2H/U_\infty = 0.12$, still another at the frequency of $f_3H/U_\infty = 0.24$, and a distant peak at the frequency of $f_4H/U_\infty = 1.28$. The first three frequencies were also deduced through a DMD decomposition applied on the same configuration (Debesse et al., 2016).

The highest frequency peak (f_4) is associated with mode numbers 68 and 69, as is evidenced in Fig. 19. It can be attributed to the Kelvin–Helmholtz mode of the mixing layer edging the separation since f_4 matches the Strouhal number of the Kelvin–Helmholtz frequency recorded experimentally by numerous authors (Bernal and Roshko, 1986; Delville, 1994), i.e. $St_\omega = f_4\delta_\omega/U_c = 0.33$, with the local vorticity thickness $\delta_\omega = (\langle U_{high} \rangle - \langle U_{low} \rangle) / \max_y \nabla \langle U \rangle$, see Fig. 16 and the local convection velocity $U_c = (\langle U_{high} \rangle + \langle U_{low} \rangle)/2$. Looking at the eigenvector intensity ϕ_u^{69} of the 69th POD mode, Fig. 19(b) confirms that this frequency corresponds to mixing layer modes.

Separated–reattached flows are characterized by two frequency modes which are related to shedding and flapping phenomena. The vortex shedding resulting from the large scale motion of the mixing layer, is characterized by a frequency peak band around $fL_R/U_\infty = 0.6 - 0.8$ (corresponding to the shedding modes, $fH/U_\infty = 0.12 - 0.16$) (Cherry et al., 1984; Kiya and Sasaki, 1983, 1985). The flapping phenomenon is an overall dynamical mechanism linked to successive enlargements and shrinkages of the separated zone. Its characteristic frequencies (corresponding to the flapping modes) are much lower than those of the shedding modes, e.g. $fL_R/U_\infty \approx 0.12$ ($fH/U_\infty \approx 0.024$) (Cherry et al., 1984; Kiya and Sasaki, 1983; 1985).

The two lowest frequencies (f_1 and f_2) are the same as those associated in the literature (Cherry et al., 1984; Kiya and Sasaki, 1985) with the recirculation bubble (the third frequency $f_3H/U_\infty = 0.24$ is simply likely to be a harmonic of $f_2H/U_\infty = 0.12$). The lowest frequency $f_1H/U_\infty = 0.04 - 0.05$ can be seen to correspond to the flapping frequency which is associated with the growth and shrinkage of the bubble (Fouras and Soria, 1995). In fact, if this frequency is renormalized with the recirculation length, we find a dimensionless frequency which matches results in the literature (Cherry et al., 1984; Kiya and Sasaki, 1985). This time scale was compared to the circulation time scale T_c associated with the main vortex within the bubble. An estimate for T_c was obtained from selecting thirty points along a characteristic streamline and computing their velocity. We found that $T_c \sim 20 - 25$, which agrees very well with the flapping frequency.

Kiya and Sasaki (1983, 1985) predict a central frequency of $fL_R/U_\infty \approx 0.6$ which is different from the one observed here when

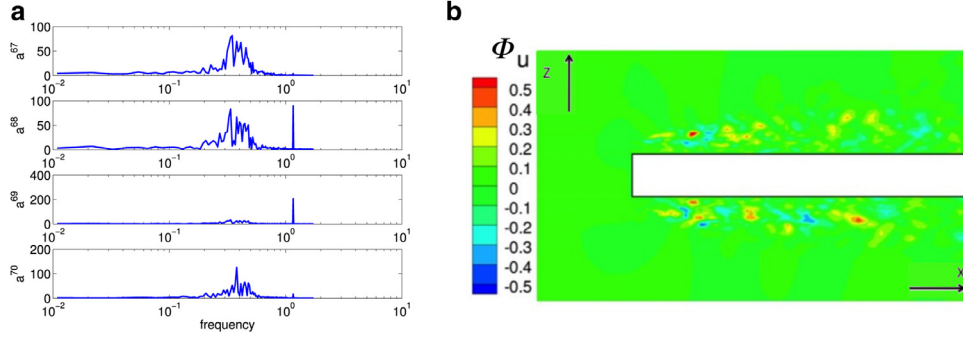


Fig. 19. Modes associated with the frequency $fH/U_0 = 1.28$: (a) Spectral density of modes from a^{67} to a^{70} (from top to bottom); (b) cross-section $y = 0$ of the eigenvector intensity of the streamwise velocity ϕ_u^n for $n = 69$.

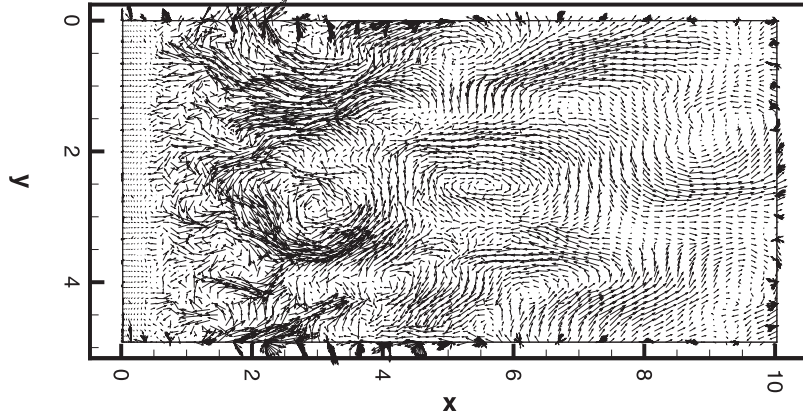


Fig. 20. Horizontal view of the second velocity POD mode at $z = 0.4H$ — the streamwise origin is located at the leading edge of the plate.

normalized with our recirculation length. However $f_2H/U_\infty = 0.12$ does match the value they found if we scale the frequency with the thickness of the plate. This makes sense as the vortex shedding process corresponds to a Karman instability (Roshko, 1955) in which the vortices interact with the wall, which creates by reflection a row of aligned vortices (not staggered, unlike a classical vortex street) of opposite sign (Sigurdson, 1995). The frequency should therefore scale with the vertical distance between the vortex and the wall, which depends on the bubble height, while the flapping frequency is associated with the recirculation time scale within the bubble, and therefore depends on the recirculation length.

All modes $n \leq 10$ were found to contain both the shedding and the flapping frequencies. It was not possible to separate both contributions in any of the modes either using Fourier transform or equivalently DMD decomposition (Debesse et al. 2016). This coupling supports the idea of a single physical origin for the two different frequencies observed.

Although both flapping and shedding are usually described as primarily two-dimensional processes, the structure of the flow is strongly three-dimensional, as illustrated in Fig. 20 by a horizontal section of the most energetic fluctuating mode. The coherence of fluctuations is especially pronounced beyond the reattachment point with an identified scale of about $L_y/3$ (i.e. a characteristic spanwise scale of $L_y/3 \sim 1.667H$).

This is confirmed by the spectral analysis (Fig. 21) that educes a characteristic wave number $k_y = 0.6$, i.e. a characteristic length scale $\lambda_y = 1.667 H$ downstream the re-attachement. More upstream ($x/L_R = 0.4, 0.6$), two more wave numbers could also be clearly identified in the spectra, leading to characteristic spanwise lengths $\lambda_y = H$ and $\lambda_y = 0.71 H$ that can be glimpsed in Fig. 20.

6.3. Surface pressure POD

POD analysis was also applied to the surface pressure along the plate. The pressure spectrum is shown in Fig. 17(b). As could be expected, since the domain is limited to a plane and only one scalar is considered, the convergence of the pressure spectrum is faster than that of the velocity. The first two modes are nearly equal, which suggests the presence of a spatio-temporal symmetry. The spectral content of the POD pressure modes can be seen to be very similar to that of the velocity counterparts. Higher-order modes are almost linearly associated with higher frequencies, with a significant low-frequency contribution observed in the first 100 modes of the field (Fig. 22(a)). In the first POD pressure modes, two main frequencies could be identified which correspond to the flapping and shedding frequencies observed for the POD velocity modes, as shown in Fig. 22(b). For the first ten modes, a peak is present at $fH/U_\infty = 0.05$, and a second one at $fH/U_\infty = 0.13$, with a significant content in the range $[0.13, 0.17]$. The Kelvin–Helmholtz frequency does not appear in the pressure spectrum. Let us recall that the pressure field is obtained at the upper surface of the plate. It is then not unexpected that the Kelvin–Helmholtz waves do not reach the surface as they are convected away from the plate. Fig. 23 shows the first four fluctuating POD pressure modes. It is clear that the two most energetic fluctuating modes are invariant in the spanwise direction. This is consistent with the aeroacoustic analysis (Green’s function analysis) performed by Debesse et al. (2016) that argued that “only the transverse mean (0th-order spanwise Fourier mode) can be efficient in driving propagative pressure fluctuations”. The idea that the wall pressure fluctuations constitute the signature of vortices is supported by application of the ex-

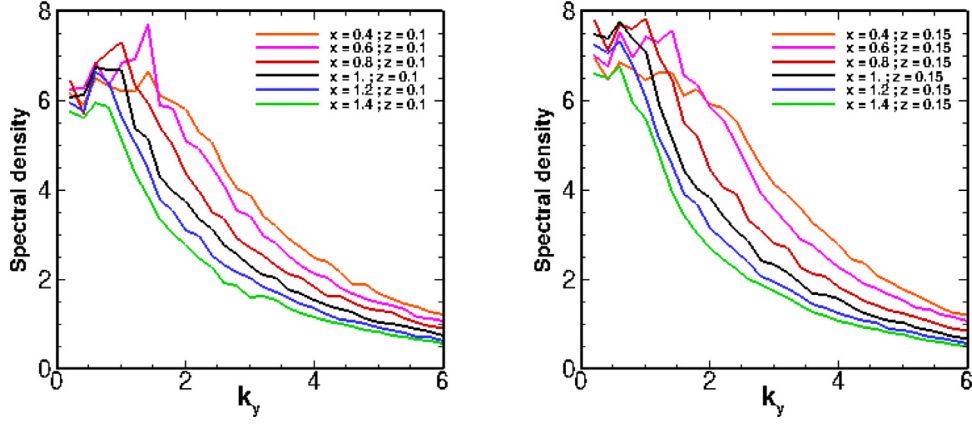


Fig. 21. Energy spectra versus the spanwise wave number of the fluctuating spanwise velocity recorded by *LES* from probes located around the centerline of the mixing layer edging the separation: $z = 0.1$ on the left and $z = 0.15$ on the right.

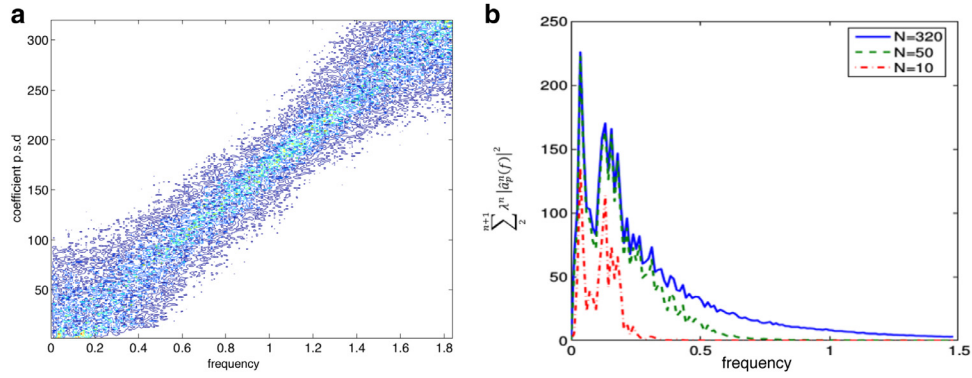


Fig. 22. The frequency is nondimensionalized with the plate thickness (a) spectral density of the pressure POD coefficients a_p^n (b) spectral density of the POD energy $\sum_{n=2}^{N+1} \lambda^n |\hat{a}_p^n(f)|^2$.

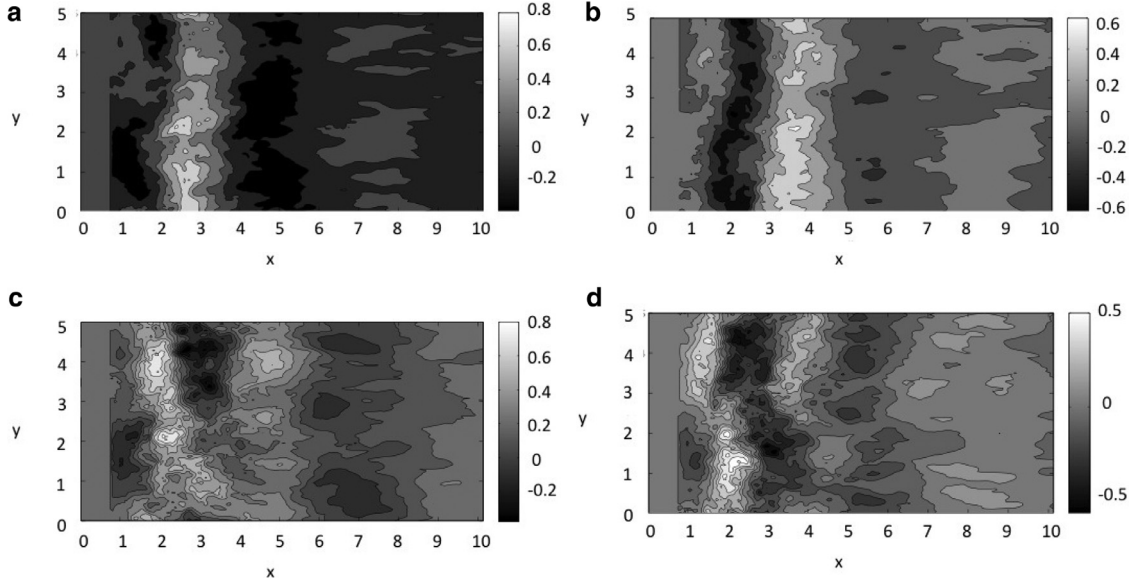


Fig. 23. Fluctuating pressure POD mode (a) $n = 2$ (b) $n = 3$ (c) $n = 4$ (d) $n = 5$ – the streamwise origin is located at the leading edge of the plate.

tended POD. The extended POD velocity modes based on the pressure were computed, using the technique first put forth by [Borée \(2003\)](#). If the n th pressure mode Φ_p^n can be written as

$$\Phi_p^n(x, y) = \sum a_p^n(t^m) p(x, y, t^m), \quad (20)$$

the corresponding extended velocity mode can be obtained from

$$\underline{\Phi}_{u(p)}^n(x, y, z) = \sum a_p^n(t^m) \underline{u}(x, y, z, t^m). \quad (21)$$

Since the pressure is almost constant in the spanwise direction (at least for the highest two fluctuating modes), it makes sense

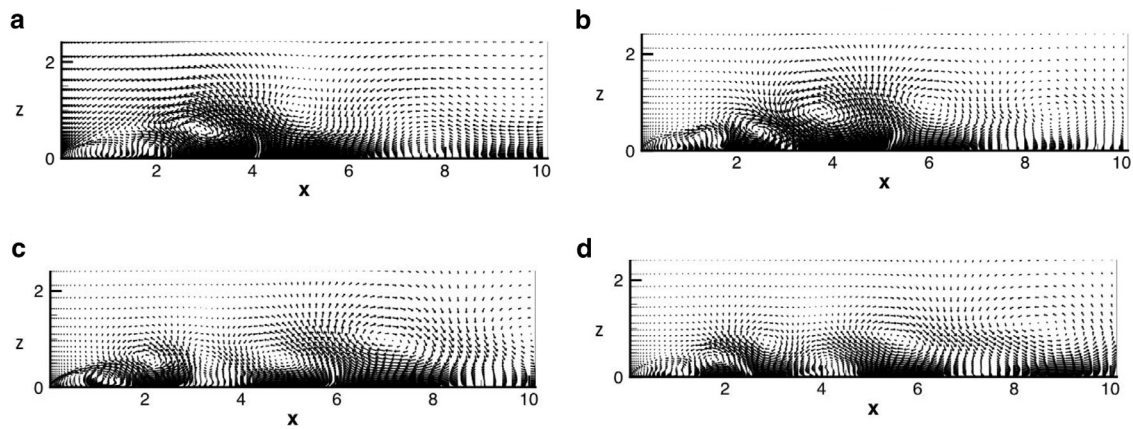


Fig. 24. Pressure-educed spanwise-averaged velocity mode (a) $n = 2$ (b) $n = 3$ (c) $n = 4$ (d) $n = 5$ – the streamwise origin is located at the leading edge of the plate.

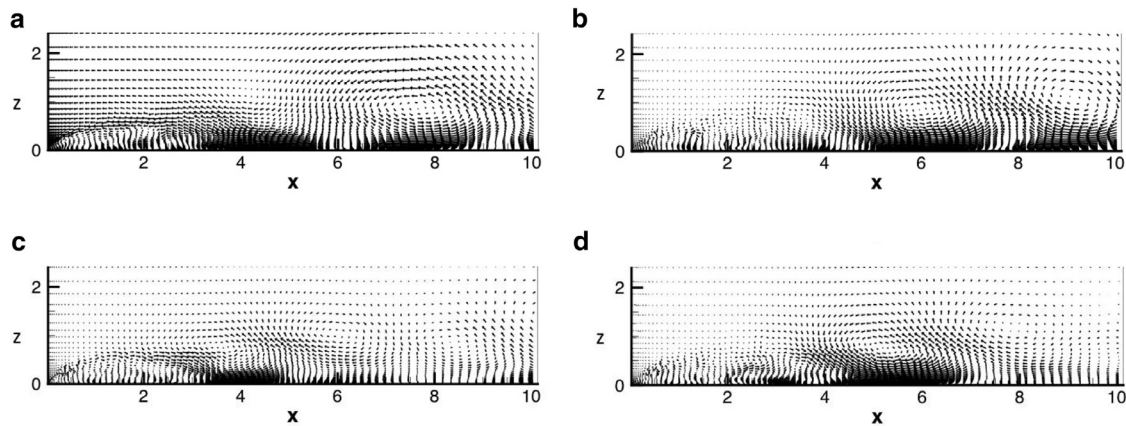


Fig. 25. Spanwise-averaged full POD velocity mode (a) $n = 2$ (b) $n = 3$ (c) $n = 4$ (d) $n = 5$ – the streamwise origin is located at the leading edge of the plate.

to look at the spanwise average of the extended velocity modes, which are represented in Fig. 24.

The first two fluctuating modes consist of a strong vortex centered above the reattachment point and convected outside the recirculation bubble. This is in good agreement with the observations of Tran (2012). The next two modes consist of a series of vortices located on either side of the reattachment point and over the entire extent of the boundary layer. The first vortex is located inside the recirculation zone. The size of the vortices increases with the streamwise distance and is about $2.5 - 3 H$ at the downstream end of the domain. The vortices are elongated and tilted at an angle of roughly 45° in the wall-normal direction. The center of the vortices is approximately located at a height of about $0.5 H$. From the position of the vortices, the first two fluctuating pressure modes ($n = 2$ and $n = 3$) appear to be related to the shedding mode, while the modes $n = 4$ and $n = 5$ could be associated with the flapping mode.

These modes can be compared with the spanwise average of the first POD velocity modes, which are represented in Fig. 25. A significant difference with the pressure modes is that the fluctuations are much less important within the recirculation zone. The first pair of modes consists of essentially two vortices separated by a distance of about $2.5 - 3 H$. The center of the vortices are located at a height of about $0.5 H$. They are located downstream of the circulation bubble. The next pair of modes consists of similar vortices but their signature is strongest closer to the recirculation zone. The general characteristics of the vortices downstream of the recirculation zone appear to be essentially the same for the velocity and the pressure-educed modes. However, the velocity vortices are less intense than the pressure-educed ones, which reflects the

lack of homogeneity due to the finite width of the vortices associated with the velocity modes.

7. Conclusions and prospects

We present resolved *LES* results of the turbulent flow generated around a blunt flat plate with a sharp leading edge, obtained with a high-order scheme. A compressible approach has been adopted to allow us to study in conjunction both the velocity and the pressure behaviors. As far as to our knowledge, it is the first time a compressible *LES* of the flow around a blunt flat plate is performed to study the separated/reattached phenomenon, we first compare these original results to the incompressible ones for validation. Results are then compared to experimental measurements coming from either PPRIME lab (Sicot et al., 2012) or previous results from the literature.

Mean and fluctuating velocity and pressure fields favorably compare to experiments when coordinates are re-scaled by using the reattachment length (L_R) as far as the Reynolds number of the computation is lower than in the experiments. The dynamic features of the separation bubble are also very well predicted since the *LES* is able to educe the shedding, the flapping and the Kelvin-Helmholtz modes as well as the growth of the turbulent mixing layer edging the separation. Some small discrepancies, very similar to those found in previous numerical studies published in the literature, are however noticeable. We suspect that the low Reynolds number used in the present simulations could affect the transition process and the turbulence development within the mixing layer which could contribute to these discrepancies. The sensitivity to the Reynolds number might be checked in a future work.

The relaxation process is also reviewed on some characteristics of the boundary layer. The distortion of the boundary layer is measured by the correlation coefficient between Reynolds stress components. While energetic mixing-layer like structures are present just downstream the reattachment, the standard values of Reynolds stress correlation coefficients are rather well recovered. A modal decomposition analysis is also proposed here to contribute to a better understanding of the coupling mechanisms between eddy structures and wall pressure fluctuations. POD and spectral analyses conducted here confirm that the most energetic motions consist of large-scale vortices shed behind the recirculation bubble. The spanwise extent of these vortices is of order H and their separation is about $\frac{1}{2}H$. These motions are characterized by two frequencies $fH/U_0 = 0.04$ and $fH/U_0 = 0.12$, which are typically associated with the flapping of the recirculation bubble, and the shedding process. While L_R/U_∞ seems to be an adequate reference time for the flapping mode, we claim that the frequency of the shedding mode better scales with H/U_∞ since it could be likely viewed as a Karman instability. The coupling between these two modes suggested by the POD supports the idea of a single origin for these two phenomena which needs more investigation for a better understanding. POD analysis of the surface pressure shows that the pressure modes are quasi-invariant in the spanwise direction that is consistent with a previous aeroacoustic analysis (Debesse et al., 2016). The vortical motions associated with the pressure modes are most intense in the reattachment region where hairpin vortices are stretched by the acceleration downstream. Through an Extended-POD technique, pressure-duced velocity modes are analyzed. In full agreement with Tran (2012), the most energetic wall pressure modes correspond to a strong vortex centered above the reattachment that has been convected outside the recirculation bubble. These most energetic wall pressure modes might be related to the shedding mode while next lower energetic wall pressure modes consisting of two same-sign vortices located on either side of the reattachment point might be related to the flapping mode.

Acknowledgement

This research is supported by the French ANR under contract No. ANR-07-BLAN-0177. Authors would like to greatly acknowledge partners of the ANR project and experimentalists from Pprime Institute, Poitiers, who recorded the experimental data-basis, for their valuable comments and discussions. Authors also greatly acknowledge the support of GENCI and the CNRS's national super-computing center (IDRIS) where part of computations have been carried out.

References

Bardina, J., Ferziger, J.H., Reynolds, W.C., 1980. Improved subgrid scale models for large eddy simulation. *AIAA Paper* 80–1357.

Bernal, L.P., Roshko, A., 1986. Streamwise vortex structure in plane mixing layers. *J. Fluid Mech.* 170, 499–525.

Borée, J., 2003. Extended proper orthogonal decomposition: a tool to analyse correlated events in turbulent flows. *Exp. Fluids* 35, 188–192.

Brown, G.L., Roshko, A., 1974. On density effects and large structure in turbulent mixing layers. *J. Fluid Mech.* 64, 775–816. Part 4

Bruno, L., Vittoria Salvetti, M., Ricciardelli, F., 2014. Benchmark on aerodynamics of rectangular 5:1 cylinder: an overview after the first four years of activity. *J. Wind Eng. Ind. Aerodyn.* 126, 87–106.

Castro, I.P., Epik, E., 1996. Boundary layer relaxation after a separated region. *Exp. Thermal Fluid Sci.* 13, 338–348.

Castro, I.P., Epik, E., 1998. Boundary layer development after a separated region. *J. Fluid Mech.* 374, 91–116.

Castro, I.P., Haque, A., 1987. The structure of a turbulent shear layer bounding a separation region. *J. Fluid Mech.* 179, 439–468.

Cherry, N., Hillier, R., Latour, M.E.M., 1984. Unsteady measurements in a separated and reattaching flow. *J. Fluid Mech.* 11, 13–46.

Comte, P., Lesieur, M., 1998. Large eddy simulations of compressible turbulent flows. Lecture Series 1998-05. *Advances in Turbulence Modelling*. Von Karman Institute

Daru, V., Tenaud, C., 2004. High order one-step monotonicity preserving schemes for unsteady flow calculations. *J. Comput. Phys.* 193, 563–594.

Daru, V., Tenaud, C., 2009. Numerical simulation of the viscous shock tube problem by using a high resolution monotonicity-preserving scheme. *Comput. Fluids* 38, 664–676.

Deardorff, J., 1970. A numerical study of three-dimensional turbulent channel flow at large Reynolds numbers. *J. Fluid Mech.* 41 (2), 453–480.

Debesse, P., Pastur, L., Lusseyran, F., Fraigneau, Y., Tenaud, C., Bonamy, C., Cavalieri, A., Jordan, P., 2016. A comparison of data reduction techniques for the aeroacoustic analysis of flow over a blunt flat plate. *Theor. Comput. Fluid Dyn.* 1–26. Submitted to

Delville, J., 1994. Characterization of the organization in shear layers via the proper orthogonal decomposition. *Appl. Sci. Res.* 53, 263–281.

Djilali, N., Gartshore, I.S., 1991. Turbulent flow around a bluff rectangular plate part i: Experimental investigation. *ASME J. Fluids Eng.* 113, 51–59.

Doris, L., 2000. Simulation des Grandes Échelles du développement spatial d'une couche de mélange turbulente compressible. Université Pierre et Marie Curie (Paris 6) Thèse de doctorat.

Doris, L., Tenaud, C., Ta Phuoc, L., 2000. LES of spatially developing 3d compressible mixing layer. *C.R. Acad. Sci. Paris t. 328, Série II b*, 567–573.

Eaton, J.K., Johnston, J.P., 1981. A review of research on subsonic turbulent flow reattachment. *AIAA J.* 19 (9), 1093–1100.

Favre, A., 1965. Equations des gaz turbulents compressibles II. Méthode des vitesses moyennes; méthodes des vitesses macroscopiques pondérées par la masse volumique. *Journal de Mécanique* 4 (4), 391–421.

Ferreira Gago, C., Brunet, S., Garnier, E., 2002. Numerical investigation of turbulent mixing in a jet/wake vortex interaction. *AIAA J.* 40 (2), 276–284.

Fouras, A., Soria, J., 1995. Large scale flapping of separated flow. In: *Proceedings of the 13th Australasian Fluid Mechanics Conference*.

Germano, M., 1992. Turbulence: the filtering approach. *J. Fluid Mech.* 238, 325–336.

Germano, M., Piomelli, U., Moin, P., Cabot, W.H., 1991. A dynamic subgrid-scale eddy viscosity model. *Phys. Fluids A* 3, 1760–1765.

Hancock, P.E., Castro, I., 1993. End effects in nominally two-dimensional separated flows. *Appl. Sci. Res.* 51 (1–2), 173–178.

Hillier, R., Cherry, N.J., 1981. The effect of stream turbulence on separation bubbles. *J. Wind Eng. Ind. Aerodyn.* 8, 49–58.

Hoarau, C., Borée, J., Laumonnier, J., Gervais, Y., 2006. Analysis of the wall pressure trace downstream of a separated region using extended proper orthogonal decomposition. *Phys. Fluids* 18 (055107).

Holmes, P., Lumley, J., Berkooz, G., 1996. *Turbulence, Coherent Structures, Dynamical Systems and Symmetry*. Cambridge University Press.

Jeong, J., Hussain, F., 1995. On the identification of a vortex. *J. Fluid Mech.* 285, 69–94.

Ji, M., Wang, M., 2010. Sound generation by turbulent boundary layer flow over small steps. *J. Fluid Mech.* 654, 161–193.

Kiya, M., Sasaki, K., 1983. Structure of a turbulent separation bubble. *J. Fluid Mech.* 137, 83–113.

Kiya, M., Sasaki, K., 1985. Structure of large-scale vortices and unsteady reverse flow in the reattaching zone of a turbulent separation bubble. *J. Fluid Mech.* 154, 463–491.

Lamballais, E., Silvestrini, J., Laizet, S., 2010. Direct numerical simulation of flow separation behind a rounded leading edge: study of curvature effects. *Int. J. Heat Fluid Flow* 31, 295–306.

Langari, M., Yang, Z., 2013. Numerical study of the primary instability in a separated boundary layer transition under elevated free-stream turbulence. *Phys. Fluids* 25, 074106.

Lenormand, E., Sagaut, P., Ta Phuoc, L., Comte, P., 2000. Subgrid-scale models for large-eddy simulations of compressible wall bounded flows. *AIAA J.* 38 (8), 1340–1350.

Lesieur, M., Comte, P., 2001. Favre filtering and macro-temperature in large eddy simulations of compressible turbulence. *C.R. Acad. Sci. Paris t. 329, Série II b*, 363–368.

Lilly, D., 1992. A proposed modification of the Germano subgrid-scale closure method. *Phys. Fluids A* 4 (3), 633–635.

Liu, S., Meneveau, C., Katz, J., 1994. On the properties of similarity subgrid scale models as deduced from measurements in a turbulent jet. *J. Fluid Mech.* 275, 83–119.

Mansour, N.N., Ferziger, J.H., Reynolds, W.C., 1978. Large Eddy Simulation of a turbulent mixing layer. Report TF. Thermosciences Div, Dept of Mech. Eng., Stanford University, CA. 11

Meneveau, C., 1994. Statistics of turbulence subgrid-scale stresses: necessary conditions and experimental tests. *Phys. Fluids* 6 (2), 815–833.

O'Neil, J., Meneveau, C., 1997. Subgrid scale stresses and their modelling in a turbulent plane wake. *J. Fluid Mech.* 349, 253–293.

Podvin, B., Quéré, P.L., 2001. Low-order p.o.d-based models for the flow in a differentially heated cavity. *Phys. Fluids* 13, 3204.

Poinsot, T.J., Lele, S.K., 1992. Boundary conditions for direct simulations of compressible viscous flows. *J. Comput. Phys.* 101, 104–129.

Roshko, A., 1955. On the wake and drag of bluff bodies. *J. Aero Sci.* 22, 124–132.

Saathoff, P.J., Melbourne, W.H., 1997. Effects of free-stream turbulence on surface pressure fluctuations in a separation bubble. *J. Fluid Mech.* 337, 1–24.

Sagaut, P., 1995. Simulations numériques d'écoulements décollés avec des modèles de sous maille. Université Pierre & Marie Curie (Paris VI) Thèse de doctorat.

Sagaut, P., 1998. Introduction à la simulation des grandes échelles pour les écoulements de fluide incompressible. Springer-Verlag.

- Sicot, C., Perrin, R., Borée, J., 2012. Wall pressure and conditional flow structures downstream of a reattaching flow region. *Int. J. Heat Fluid Flow* 35, 119–129.
- Sigurdson, L., 1995. The structure and control of turbulent reattaching flow. *J. Fluid Mech.* 298, 205–234.
- Sirovich, L., 1987. Turbulence and the dynamics of coherent structures part I: coherent structures. *Quart. Appl. Math.* 45 (3), 561–571.
- Smagorinsky, J., 1963. General circulation experiments with the primitive equations I : the basic experiments. *Month. Weath. Rev.* 91 (3), 99–165.
- Tafti, D.K., Vanka, S.P., 1991. A three-dimensional numerical study of flow separation and reattachment on a blunt plate. *Phys. Fluids A3* (12), 2887–2909.
- Tenaud, C., Ta Phuoc, L., 1997. LES of unsteady compressible separated flow around NACA 0012 airfoil. In: Kutler, P., Flores, J., Chattot, J. (Eds.), *Lecture Notes in Physics*. In: 15th International Conference on Numerical Methods in Fluid Dynamics, Monterey, Vol. 490, pp. 424–429. CA, June 1996
- Tran, T., 2012. Modélisation hybride RANS/LES d'écoulement massivement décollés en régime turbulent. Etude des corrélations pression/vitesse et confrontation à l'expérimentation. Ecole Nationale Supérieure de Mécanique et d'Aérotechnique (ENSMA), Poitiers, France Thèse de doctorat.
- Vreman, B., Geurts, B., Kuerten, H., 1995. A priori tests of large eddy simulation of the compressible plane mixing layer. *J. Eng. Math.* 29, 299–327.
- Yang, J., Perng, Y., Yen, R., 1999. Implicit weighted essentially non-oscillatory schemes for the compressible Navier–Stokes equations. *AIAA J.* 39 (11), 2082–2090.
- Yang, Z., Abdalla, I.E., 2009. Effects of free-stream turbulence on a transitional separated-reattached flow over a flat plate with a sharp leading edge. *Int. J. Heat Fluid Flow* 30 (5), 1026–1035.
- Yang, Z., Voke, P.R., 2000. Large-eddy simulation of separated leading-edge flow in general co-ordinates. *Int. J. Meth. Eng.* 49, 681–696.
- Yang, Z., Voke, P.R., 2001. Large-eddy simulation of boundary-layer separation and transition at a change of surface curvature. *J. Fluid Mech.* 439, 305–333.